Cis-trans Isomerization is Not Rate Determining for b_2 Ion Structures: A Guided Ion Beam and Computational Study of the Decomposition of $H^+(GlyProAla)$

Roland M. Jones III, Georgia C. Boles, and P. B. Armentrout*

Department of Chemistry, University of Utah, 315 S.1400 E. Rm 2020, Salt Lake City, UT 84112, United States

Abstract

Decomposition of the protonated tripeptide, GlyProAla (H⁺GPA), through collision-induced dissociation with Xe in a guided ion beam tandem mass spectrometer (GIBMS) is examined. Cross sections for the formation of [b₂]⁺, [y₂ + 2H]⁺, [a₁]⁺, [b₃]⁺, [a₃]⁺, [a₂]⁺, and H⁺(1-pyrroline) fragment ions were collected as a function of kinetic energy. Analysis of these cross sections include consideration of the effects of multiple collisions, dissociation lifetimes, reactant internal and kinetic energy distributions, competition among channels, and evolution into sequential channels. Structures and molecular parameters of reactants, transition states, intermediates, and products were identified using the B3LYP/6-311+G(d,p) level of theory, with single-point energy calculations performed at the B3LYP, B3P86, and MP2(full) levels of theory using a 6-311+G(2d,2p) basis set. Good agreement between experimental threshold energies and those calculated for rate-limiting transition states allow key reaction pathways for the formation of each product to be identified. The MP2(full) level of theory is found to agree best with the experimental results. Notably, even though H⁺GPA starts with a cis-peptide bond, it forms an oxazolone as its [b₂]⁺ fragment and the absence of a diketopiperazine [b₂]⁺ fragment is verified by other key observations.

Keywords: ab initio calculations; diketopiperazine; peptides; oxazolone; thermochemistry

Dedicated to Bill Hase, a great scientist, scientific leader, and someone who could talk to experimentalists.

Introduction

Peptide sequencing is a key process in identifying unknown proteins and their subunits. More specific applications include sequencing the human proteome, identification of biomarkers for medical diagnosis, and general characterization of proteins [1, 2]. As a result, there is a demand for efficient and robust sequencing techniques. Tandem mass spectrometry (MS/MS) has commonly been used as a sequencing method by analyzing the fragmentation pathways of protonated gas-phase peptides through collision-induced dissociation (CID). Mass identification of the resulting peptide fragments is used to help elucidate the original peptide sequence [3]. In an attempt to make MS/MS peptide sequencing more efficient and robust, studies have been geared toward developing sequencing algorithms that compare different CID spectra with a database to help identify the sequence [4-8].

Currently, most algorithms do not include intensity information and focus on peaks corresponding to $[b_n]^+$ (containing the N-terminus) and $[y_n + 2H]^+$ (containing the C-terminus) sequence fragments [4] (where we adopt the all-explicit nomenclature of Chu et al. [9]). Yet, intensity information, which includes information about competition among reaction pathways [10], has the potential to enhance the sequence identification of less ordered proteins. Furthermore, analyzing different fragment types (e.g., $[a_n]^+$ and internal ions) could enhance the completeness of peptide sequencing, especially when low amounts of $[b_n]^+$ and $[y_n + 2H]^+$ fragments are found. A good example is the study by Zenaidee et al. who found that the inclusion of internal ions in their algorithms increased the sequencing of carbonic anhydrase II and ubiquitin from ~50% to ~99% [11]. Generally, it is thought that peptide fragmentation relies on the intramolecular migration of an excess proton to create conformers capable of undergoing rapid fragmentation, i.e., the "mobile proton" model, governed by charge-directed mechanisms [10, 12, 13]. Past studies have strongly suggested that the proton often migrates to a peptide backbone amide nitrogen, which enables cleavage of amide bonds to form the $[b_n]^+$ or $[y_n + 2H]^+$ sequence ions [10, 12, 14-16]. Addition of more energy to the system can result in these primary product ions undergoing further decomposition, or species produced from charge-remote (i.e., no proton movement) dissociation pathways may arise [12].

Previous work has shown that protonated peptides containing proline exhibit a higher propensity for fragmenting into $[y_n + 2H]^+$ ions, a phenomenon often referred to as the proline effect, which was originally attributed to the proton affinity of the tertiary amide [17, 18]. Studies conducted by Loo et al. suggested that the proline amide bond dissociates more easily than other amide bonds [19]. In contrast, CID studies conducted by Vaisar and Urban suggested that the higher amount of $[y_n + 2H]^+$ ions can be attributed to the ring strain in the resulting $[b_n]^+$ ions [20]. In the case of protonated tripeptides having proline as the central residue surrounded by glycine and/or alanine, fragmentation mostly occurs through the peptides on the C-terminal side of the proline and produces $[b_2]^+$ and $[a_2]^+$ ions [21].

The tripeptide of interest in this study, protonated GlyProAla (H⁺GPA), is one such species. Wysocki and co-workers have previously studied its decomposition and found that one of its predominant products is the $[b_2]^+$ ion [22]. Infrared multiple photon dissociation (IRMPD) action spectroscopy studies show that this $[b_2]^+$ product has a five-membered ring oxazolone (Oxa) structure. Interestingly, by changing the identity of the N-terminal residue from Gly, the structure of the [b₂]⁺ product can be altered to a six-membered ring, protonated diketopiperazine (H⁺DKP), or a mixture of the two structures [22]. For both Oxa and H⁺DKP structures, because proline is the central residue, the $[b_2]^+$ products are bicyclic. In the case of the Oxa $[b_2]^+$ structure, it was originally thought the bicyclic ring would be too energetically prohibitive [12, 20], but theoretical calculations by Grewal et al. demonstrated this was not the case [21]. Other studies have suggested that forming an Oxa [b₂]⁺ ion usually requires a trans configuration for the peptide bond of the N-terminus, whereas forming the H⁺DKP structure requires a *cis* configuration of this bond [23-26]. In this context, H⁺GPA is interesting because its [b₂]⁺ product takes on exclusively the Oxa structure despite the fact that proline favors a cis configuration for its lowest-energy conformer in the gas phase [22, 27]. Furthermore, the exclusive formation of Oxa $[b_2]^+$ ions suggests that cis/trans isomerization does not limit the rate of this channel. In addition, Oxa formation must be favored kinetically because the Oxa product is calculated to be 48 kJ mol⁻¹ higher in energy than the H⁺DKP product [22]. This is further evident in work from Paizs and Suhai [23] who deduced that the pathway for formation of H⁺DKP from a similar tripeptide, H⁺GGG, required that the first peptide bond needed to undergo a *trans/cis* isomerization and that this process was energetically feasible (although statistical Rice-Ramsperger-Kassel-Marcus (RRKM) theory was used to show it was slow). Rather, a step later in the process of formation of H⁺DKP was shown to have a much higher barrier than formation of Oxa. This conclusion was later confirmed experimentally by Armentrout and Clark for the H⁺GGG [b₂]⁺ ion [26]. These observations suggest that the preference for a *cis* or *trans* configuration in the first peptide bond is not predictive for whether [b₂]⁺ ion formation yields a [b₂]⁺ fragment having the Oxa versus H⁺DKP structure, but the kinetics of such an isomerization might influence what is observed.

The study presented here extends the previous work on H⁺GPA by providing more quantitative information that can be used in a detailed analysis of the reaction mechanisms. This is accomplished through measurement of the energetics for product formation from the dissociation of H⁺GPA using a guided ion beam tandem mass spectrometer (GIBMS). Threshold energies for seven dissociation pathways observed in the experiments are obtained. These values are compared to single-point energies of the rate-limiting transition states (TSs) calculated using several levels of theory. Good agreement between the theoretical and experimental values validates the proposed mechanisms and identifies the structures of the products formed. Furthermore, the present work creates a benchmark for comparison to decomposition studies of other peptide sequences in order to identify key mechanistic differences and how these differences depend on specific sequences.

Experimental and Computational Details

General Experimental Procedures

Cross sections of H⁺GPA undergoing collisions with Xe were measured using a GIBMS described in previous work [28-30]. The gas-phase H⁺GPA ions were generated using an electrospray ionization (ESI) source [31] under ambient conditions. The sample solution consisted

of 50:50 by volume of $H_2O/MeOH$ (Sigma-Aldrich) with ~ 10^{-4} M GPA (Indofine Chemical). The solution flow rate was set to 0.05 mL/hour, and the ESI needle voltage ranged from ~1700 - 2200 V. The ions were directed by a capillary heated to 80 °C into a radio frequency (rf) ion funnel [32], in which they were collimated into a tightly focused beam and injected into an rf hexapole ion guide, which radially trapped the ions. In order to analyze higher order decomposition products, some experiments utilized an in-source fragmentation method [33] to decompose H^+GPA in the hexapole. Briefly, six brass electrodes were placed between the hexapole rods in the high-pressure region. A DC voltage applied to these electrodes pulled the ions closer to the rods where rf heating ensued and dissociated the H^+GPA to form the primary product, $[b_2]^+$. In either case, the H^+GPA or $[b_2]^+$ ions underwent multiple thermalizing collisions (> 10^4) with ambient gas at a pressure near 10^{-2} Torr that also entered the instrument through the capillary. Thus, these reactant ions had internal energies that are described by a Maxwell-Boltzmann distribution of rovibrational states at 10^{-2} Torr that are described by a Maxwell-Boltzmann distribution of rovibrational states at 10^{-2} Torr than a previously demonstrated, 10^{-2} Torr 10^{-2} Torr

Ions were extracted from the hexapole guide, focused into a magnetic momentum analyzer where the H⁺GPA or $[b_2]^+$ ions were selected, decelerated to a well-defined kinetic energy using an exponential retarder, and focused into a meter-long dual rf octopole guide where they were radially trapped [29, 41, 42]. The octopole passed through a static gas cell holding Xe as a collision gas at a low enough pressure that single collision conditions dominated. Nevertheless, cross sections were obtained at several pressures (0.3, 0.15, and \sim 0.05 mTorr) and extrapolated to zero pressure before data analysis. Collisions resulted in the formation of product ions that drifted along with residual reactant ions to the end of the octopole where they were focused into a quadrupole mass filter for mass analysis. Ions were then detected using a Daly detector [43], and signals were processed using standard counting techniques. Product and reactant ion intensities were converted to absolute cross sections and the ion kinetic energies in the laboratory frame were converted to relative energies in the center-of-mass (CM) frame using methods detailed previously [28, 30]. In this manuscript, all energies are presented in the center-of-mass (CM) frame.

Data Analysis

The thermochemical data analysis procedure has been well described in previous studies [44-46], and further details can be found in the Supplementary Data. Briefly, cross sections were modeled competitively using Eq. (S1), which accounts for the kinetic energy of the reactants, the energy deposition efficiency, the energies of populated rovibrational states of the reactant ion, and the probability for dissociation of the energized molecule within the time-of-flight (\sim 5 × 10⁻⁴ s) [29]. Furthermore, Eq. (S1) accounts for competition among parallel dissociation pathways using statistical factors associated with the rate constant for an individual product channel relative to the rate constant for all processes, both determined by RRKM theory, as detailed in Eq. (S2) [47, 48]. Finally, Eq. (S1) was convoluted over the distribution of kinetic energies of the reactants before comparison with the data. A nonlinear least-squares procedure was then used to optimize the various adjustable parameters. This procedure produces energy thresholds at 0 K for each decomposition pathway [30, 44-46, 49-51]. Uncertainties in the parameters include variations among data sets, in the value of n, in the time available for dissociation, in the vibrational frequencies of the reactant and TSs, and the uncertainty in the energy scale.

Computational Details

Possible ground structures (GSs) of reactants and products were identified with a simulated annealing program using the Amber 14 force field. Relaxed potential energy surface scans at the B3LYP/6-31G(d) [52-54] level of theory were then used to search for conformers and isomers of reactants, transition states (TSs), intermediates, and products. These structures were optimized further to obtain vibrational frequencies and rotational constants at the B3LYP/6-311+G(d,p) level of theory with a Berny optimization [55]. Single-point energies were calculated at the B3LYP, B3P86, and MP2(full) (where full refers to the correlation of all electrons, abbreviated as MP2 below) levels of theory with the 6-311+G(2d,2p) basis set. Zero-point energy corrections were applied to all single-point energies using the B3LYP/6-311+G(d,p) frequencies with a scaling constant of 0.989 [56]. These levels of theory and basis sets have previously been shown to provide accurate comparison with experimental energies in studies of protonated glycine [57], protonated

diglycine [24, 34], protonated triglycine (H⁺GGG) [15], protonated GlyAlaGly (H⁺GAG) [16], and [b₂]⁺ species [26].

Nomenclature

The nomenclature used here follows that outlined in previous studies of H⁺GGG and H⁺GAG [15, 16]. Briefly, H⁺GPA conformers are named with a system that identifies the protonation site enclosed in square brackets followed by the eight dihedral angles going from the N-terminus along the backbone to the C-terminus: $\angle N^1CCN^2$, $\angle CCN^2C$, $\angle CN^2CC$, $\angle N^2CCN^3$, $\angle CCN^3CC$, $\angle N^3CCO^4$, and $\angle CCO^4H$. Here superscripts 1, 2, and 3 denote the residues glycine, proline, and alanine, respectively. Superscript 4 denotes the hydroxyl oxygen on the C-terminus where a fourth peptide bond would begin. The dihedral angles are labeled as c (cis) for angles < 45°; g (gauche) for angles that fall between 45° and 135°; and t (trans) for angles > 135°. Product conformers are also named using this nomenclature system.

Transition states are denoted by TS followed by a description of the protonation site, dihedral angle, or bond cleavage undergoing transformation. Proton movements are denoted with a dash (-) between the two designated atoms in square brackets, a dihedral angle change is denoted within parentheses, and a bond cleavage is indicated by \sim inside curly brackets. In all cases, the lower energy conformer is listed first. For example, $TS[N^1-O^4]$ denotes a proton transfer from the N-terminus (the lower energy conformer) to the C-terminus. Likewise, (gt) indicates an angle switching from a *gauche* (the lower energy conformer) to a *trans* conformation, and the TS for an amide bond breakage is denoted $TS\{C\sim N^3\}$. Although more complicated than some nomenclatures for peptides, this system has proven effective for distinguishing structures and pathways [15, 16, 24, 26, 57].

Results

Cross Sections for Collision-Induced Dissociation of H⁺GPA

Figure 1 shows the experimental kinetic energy dependent cross sections collected for the decomposition of H⁺GPA by collision with Xe at 0.12 mTorr. Fragmentation of H⁺GPA produced

seven different observable ionic products. On the basis of the theoretical results (see below), these are assigned to reactions (1) - (7).

$$H^{+}GPA + Xe \rightarrow C_{10}H_{16}N_{3}O_{3}^{+}([b_{3}]^{+}, H^{+}GPMOx) + H_{2}O + Xe$$
 (1)

$$\rightarrow C_9 H_{16} N_3 O_2^+ ([a_3]^+) + H_2 O + C O + X e$$
 (2)

$$\rightarrow C_8H_{15}N_2O_3^+([y_2+2H]^+, H^+PA) + CO + CH_2NH + Xe$$
 (3)

$$\rightarrow$$
 $C_7H_{11}N_2O_2^+([b_2]^+, AMPO_X^+) + C_3H_7NO_2(A) + Xe$ (4a)

$$\rightarrow$$
 $C_7H_{11}N_2O_2^+([b_2]^+, AMPOx^+) + C_2H_4NH + H_2O + CO + Xe$ (4b)

$$\rightarrow C_6H_{11}N_2O^+([a_2]^+) + CO + C_3H_7NO_2(A) + Xe$$
 (5a)

$$\rightarrow C_6H_{11}N_2O^+([a_2]^+) + 2CO + H_2O + C_2H_4NH + Xe$$
 (5b)

$$\rightarrow$$
 C₄H₇NH⁺(H⁺(pyr)) + 2 CO + C₃H₇NO₂ (A) + CH₂NH + Xe (6a)

$$\rightarrow$$
 C₄H₇NH⁺(H⁺(pyr)) + C₂H₄NH + 3 CO + CH₂NH + H₂O + Xe (6b)

$$\rightarrow$$
 CH₂NH₂⁺([a₁]⁺) + CO + C₈H₁₄N₂O₃ (PA) + Xe (7a)

$$\rightarrow$$
 CH₂NH₂⁺([a₁]⁺) + C₃H₇NO₂ (A) + 2 CO + C₄H₇N + Xe (7b)

$$\rightarrow$$
 CH₂NH₂⁺([a₁]⁺) + C₂H₄NH + 3 CO + C₄H₇N + H₂O + Xe (7c)

The results of Figure 1 demonstrate that reactions (4a) and (1) have the lowest apparent threshold energies. These products, $[b_2]^+$ and $[b_3]^+$ are shown below to have aminomethyl-1-pyrrolo-5-oxazolone, AMPOx⁺, and protonated 1-glycyl-2-pyrrolo-4-methyl oxazolone, H⁺GPMOx, structures, respectively. They both dissociate at higher energies by losing CO to form $[a_2]^+$ in reaction (5a) and $[a_3]^+$ in reaction (2), respectively. Experimental evidence for this sequential decarbonylation is the decline in the $[b_2]^+$ cross section as the $[a_2]^+$ cross section rises. Formation of $[y_2 + 2H]^+$, protonated ProAla (H⁺PA), in reaction (3) must also be a primary process. At even higher energies, $[a_2]^+$ can further decompose in reaction (6a) to form m/z 70, identified below as H⁺(pyrroline) and abbreviated as H⁺(pyr). This sequence, $[b_2]^+ \rightarrow [a_2]^+ \rightarrow H^+(pyr)$, is demonstrated by the smooth appearance for the sum of these three cross sections, Figure 1. Further, $[a_3]^+$ can lose C_2H_4NH to form $[b_2]^+$ as a tertiary product in reaction (4b), which can then dissociate to $[a_2]^+$ in reaction (5b) and to H⁺(pyr) in reaction (6b). The product ion with the highest threshold energy, $CH_2NH_2^+$ $[a_1]^+$, can be formed by many pathways, with that having the lowest energy being the

primary fragmentation of reaction (7a), which competes with reaction (3). Further decomposition of the $[b_2]^+$ product via reactions (7b) and (7c), which compete with reactions (6a) and (6b), respectively, also yield $[a_1]^+$. These various pathways are collected in Scheme 1.

Overall, the experimental results of Figure 1 are similar to those from Grewal et al. where they observed that H*GPA yielded major ions (>10%) of $[b_2]^+$, $[a_2]^+$, and $[y_2 + 2H]^+$ fragments having 54, 22, and 16% of product ions, respectively, at 3 eV (CM) for "single-collision" CID with Ar or N₂ [21]. This product distribution is similar to our results near 4.5 eV. For metastable ion decomposition using a BE double-focusing mass spectrometer [21], they found that H*GPA formed $[b_2]^+$, $[b_3]^+$, and $[y_2 + 2H]^+$ fragments with 61, 27, and 12% of the ion signal, respectively, similar to our distribution near 2.5 eV. In neither experiment was the presence of $[a_1]^+$, $[a_3]^+$, or H*(pyr) ions reported [21], consistent with the elevated thresholds or low abundances here (Figure 1). Neither the study of Grewal et al. or ours observed the $[y_1 + 2H]^+$ product. In this same study, decomposition of the related peptide, H*GPG, was reported over a more extensive energy range, and there $[b_2]^+$ (45 %), $[a_2]^+$ (24 %), $[y_2 + 2H]^+$ (22%), $[b_3]^+$ (<10 %), $[a_1]^+$ (<10 %), and m/z 70 fragments (<10 %) at 3 eV (CM) were observed, and their products had energy profiles similar to those of Figure 1 [21]. Like our product distribution near 3 eV, metastable fragmentation yielded only $[b_2]^+$ (61%), $[b_3]^+$ (19%), $[y_2 + 2H]^+$ (16%), and $[a_2]^+$ (5%), similar to their findings for H*GPA with the addition of $[a_2]^+$.

Cross Sections for Collision-Induced Dissociation of [b₂]⁺

In order to further characterize the dominant $[b_2]^+$ product ion and its subsequent decomposition from other reaction pathways, a previously described in-source fragmentation method [33] (noted above) was used to generate the $[b_2]^+$ product from electrosprayed H⁺GPA. This product ion was then mass selected and subjected to CID with Xe, thereby examining the $[b_2]^+$ decomposition pathways directly. This also allows us to model additional product formation pathways, as described below. Figure 2 illustrates the kinetic-energy-dependent cross sections for CID of the $[b_2]^+$ ion with Xe extrapolated to zero pressure. The $[a_2]^+$, $[a_1]^+$, and H⁺(pyr) fragments form with appreciable intensity. The $[a_2]^+$ cross section clearly decreases in intensity as the other

two rise, consistent with the $H^+(pyr)$ and $[a_1]^+$ fragments being formed sequentially from the $[a_2]^+$ fragment. Further, the $H^+(pyr)$ cross section does not lose much intensity as the $[a_1]^+$ cross section appears. This behavior suggests that $H^+(pyr)$ and $[a_1]^+$ formations are parallel reaction pathways with 1-pyrroline having a higher proton affinity than CH_2NH , a conclusion that is tested below by modeling and theory. Comparison of these cross sections with those for the same species in Figure 1 indicates that all three H^+GPA product ions probably have significant contributions through the $[b_2]^+$ decomposition pathway, reactions (5a), (6a), and (7b), although the $H^+(pyr)$ cross section in Figure 1 is larger compared to the $[a_1]^+$ cross section, suggesting that another pathway for $H^+(pyr)$ formation, reaction (6b) via $[y_2 + 2H]^+$, may also be active. Relative threshold energies in Figure 1 are roughly consistent with displacement upwards by the threshold energy for formation of $[b_2]^+$, although the sequential $H^+(pyr)$ and $[a_1]^+$ ions are shifted to somewhat higher energies in Figure 1. Such differences can be associated with the different internal energy distributions of the $[b_2]^+$ ions formed as a reactant and as a primary product from H^+GPA . Overall, the comparisons suggest that decomposition of the primary $[b_2]^+$ product is the dominant contributor to the formation of the $[a_2]^+$ and $H^+(pyr)$ ions in Figure 1.

H⁺GPA Ground Structure

The Supporting Data contains a thorough theoretical exploration of possible conformers of H^+GPA . The results are summarized in Figure 3 with the ground structure (GS) being [N¹]-tcgctgtt. Note that the peptide bond between Gly and Pro (second dihedral angle) is cis, which positions the protonated N-terminus toward the C-terminus, thereby enabling hydrogen bonds between N¹ and the O¹ and O³ carbonyl oxygens (N¹H•O¹C and N¹H•O³C). Additionally, there is a hydrogen bond between N³ and N² (N³H•N²). The lowest energy excited conformer is [N¹]-gccttgtt, identified by Grewal et al. as the GS of a similar peptide, H⁺GPG, using free energy calculations at 298 K with the B3LYP/6-31++G(d,p) level of theory [21]. A 298 K Maxwellian distribution of the two conformers at room temperature predicts that the [N¹]-tcgctgtt GS conformer would comprise 89 – 98% of the H⁺GPA ions present. We also investigated the possibility of the Ala peptide bond (\angle CCN³C) exhibiting a cis configuration, as in [N¹]-gcctcgtt, and O¹ being protonated, [O¹]-

tcggtgtt, Figure 3. Other higher energy conformers can be found in Supplementary Table S2.

Finally, we also looked for conformers having the Pro peptide bond adopting a *trans* configuration, finding [N¹]-gtgttgtt as the lowest *trans*-Pro conformer (Figure 3). A full potential energy surface connecting this conformer with the GS can be found in Supplementary Figure S1. The rate-limiting step is the *cis/trans* isomerization barrier at TS(H⁺GPA[N¹]-g(ct)(cg)ttgtt), Figure 3, which lies 80 – 84 kJ mol⁻¹ above the GS and 42 – 53 kJ mol⁻¹ above [N¹]-gtgttgtt. Such a barrier could kinetically trap *trans*-Pro isomers during reactant ion formation, as has been found in studies of H⁺GPGG [27, 58]. The possible presence of such trapped *trans*-Pro isomers in this study is evaluated below by comparing the experimental and theoretical energies needed for the decompositions of H⁺GPA.

$\lceil b_2 \rceil^+$ Formation

The formation of $[b_2]^+$ ions from H⁺GPA has a mechanism that parallels that for H⁺GGG and H⁺GAG described in previous studies [15, 16, 59, 60]. Supplementary Figure S2 shows the potential energy surface for $[b_2]^+$ formation beginning with $[N^1]$ -gtgttgtt (final product of *cis/trans* isomerization) and Table S3 lists the energies of all intermediates and TSs. Briefly, the GS must isomerize to $[N^1]$ -gccttgtt through several dihedral angle rotations, followed by the *cis/trans* isomerization at the Gly-Pro peptide bond to form $[N^1]$ -gtgttgtt. This is followed by the N-terminus moving closer to the C-terminus, which allows proton transfer from N^1 to N^3 through TS(H⁺GPA[N¹-N³]) and forms the intact Ala leaving group. Another dihedral angle rotation positions O^1 to attack CO^2 as a nucleophile through TS(H⁺GPA[N³]-(gt)tcgtgtt{ $O^2C\sim N^3$ }) leading to AMPOx⁺, Figure 4, and Ala products. Theoretical calculations indicate that the AMPOx⁺ ($[b_2]^+$) + Ala product asymptote lies 160 - 209 kJ mol⁻¹ above the GS, Table 1, and that it can be formed with no intervening TSs at higher energies. Thus, reaction (4) is limited by a loose phase space limit (PSL) TS, explaining why this product is formed efficiently, Figure 1.

We also identified a rate-limiting TS for formation of H⁺DKP [b_2]⁺, protonated octahydropyrrolo[1,2-a]piperazine-1,4-dione, which forms via the tight TS(H⁺GPA[O¹,N¹-N³]-(ge)c(ge)tgttt{CO²~N³}), Figure 5. In this TS, O¹ is protonated and an [N¹-N³] proton transfer,

covalent bond formation between N¹ and CO², and cleavage of the Ala peptide bond (CO²~N³) all occur in a concerted manner. This TS lies 249 – 263 kJ⁻¹ above the GS and 103 – 152 kJ mol⁻¹ above the product asymptote, Table 1. As such, even though H⁺DKP lies 49 – 54 kJ mol⁻¹ below AMPOx⁺, the PSL TS for Oxa formation is favored entropically and enthalpically (by 49 – 103 kJ mol⁻¹) over the tight TS for H⁺DKP formation. Consequently, no H⁺DKP [b₂]⁺ is expected to be observed, consistent with the IRMPD findings of Wysocki and coworkers [22]. A reviewer questioned whether a TS in which N³ was protonated before the nucleophilic attack of N¹ at the CO² carbon might be viable. We had attempted to explore such a pathway several times but as N¹ approaches the carbon, it is sufficiently close to N³ that proton transfer to N¹ occurs first, preventing this nucleophilic approach.

When comparing the Oxa pathway with those for the formation of other [b₂]⁺ ions [15, 59-61], there are two key differences. First, our calculations determine that the H⁺GPA GS in the gas phase favors a *cis*-Pro configuration, whereas tripeptide systems without proline (H⁺GGG, H⁺GAG, and H⁺GFG) have a GS with the first peptide bond adopting a *trans* configuration [15, 16, 21]. In all cases, theoretical calculations indicate that this *trans* configuration is essential for Oxa formation as this positions the N-terminus to allow transfer of its proton to N³ and for O¹ to act as a nucleophile. Hence, the *cis/trans* isomerization is required in the present system. Once the *trans* conformer is achieved in H⁺GPA, the reaction pathway is mostly consistent with those of H⁺GGG [15] and H⁺GAG [16]. Second, the mobile proton is transferred directly from the N¹-terminus to N³ in H⁺GPA, whereas H⁺GGG and H⁺GAG show the mobile proton being passed from N¹ to O¹ before moving to [N³] [15, 16, 59-61]. In the case of H⁺GPA, the N-terminus does not transfer the proton to the oxygen because the Pro sidechain sterically hinders the movement of [O¹].

Lack of $[y_1 + 2H]^+$ Product

The $[y_1 + 2H]^+$ product was not observed in decomposition of H⁺GPA, either here or in previous work [21]. Normally, formation of the $[y_1 + 2H]^+$ product from protonated tripeptides competes directly with $[b_2]^+$ formation, as both products arise from the cleavage of the peptide

bond at $O^2C\sim N^3$ [15, 16]. The mobile proton is shared by the two incipient fragments, and whichever has the higher proton affinity can be formed at lower energies and generally dominates the product spectrum. In contrast, the bicyclic AMPOx⁺ [b₂]⁺ product from H⁺GPA has a quaternary nitrogen because of the proline ring and therefore has no proton that is easily transferred to the Ala fragment to form [y₁ + 2H]⁺. In contrast, the H⁺DKP [b₂]⁺ structure, Figure 5, should exhibit a more facile proton transfer and would likely produce the [y₁ + 2H]⁺ product. As a result, the lack of the [y₁ + 2H]⁺ product is further evidence that no H⁺DKP is present.

Decarbonylation from $[b_2]^+$ *to* $[a_2]^+$

As shown in Figure 2, the Oxa [b₂]⁺ product undergoes decarbonylation to form the [a₂]⁺ fragment. This process is of particular interest because the $[a_2]^+$ structure and energetics may help characterize the structure of the $[b_2]^+$ product. Schematics of the mechanism for further decomposition of both $[b_2]^+$ structures are provided in Scheme 2, and the energetics are compared in Table 2. For the oxazalone structure, a representative reaction potential energy surface can be found in Supplementary Figure S3. Mechanistically, decarbonylation of the [b₂]⁺ AMPOx⁺ structure occurs by detaching the CO from the five-membered ring TS(AMPOx⁺{C~CO²~O¹}), which forms glycyldihydropyrrol-1-ium with a double bond on the pyrrole ring, Figure 4. Because the charge is localized on a quaternary nitrogen, no proton movement is needed to initiate this process. Theoretical calculations indicate that this TS lies 268 -312 kJ mol^{-1} above the H⁺GPA GS, Table 2. The $[a_2]^+$ + Ala + CO products of reaction (5a) lie 196 – 254 kJ mol⁻¹ above the H⁺GPA GS and 51 – 72 kJ mol⁻¹ below the TS, such that the TS is rate-limiting for this process. Notably, the energy required for $[a_2]^+$ formation from the AMPOx⁺ precursor is not enough to allow further decarbonylation according to all three levels of theory. As a result, the [a₂]⁺ cross section can build in intensity before the second decarbonylation occurs at 38 – 89 kJ mol⁻¹ higher energies, Table 2.

For H⁺DKP, a reaction potential energy surface can be found in Supplementary Figure S4. Here, decarbonylation of H⁺DKP is initiated by proton migration from O¹ to either amide in the six-membered ring via TS(H⁺DKP[O¹-N¹]) or TS(H⁺DKP[O¹-N²]), Figure 5. These TSs are

similar in energy (Table 2) and rate limiting for $[a_2]^+$ formation at most levels of theory, as also seen in previous work for the H⁺DKP structures associated with H⁺GGG and H⁺GAG [26]. The proton migration weakens the bond to the amide such that loss of CO occurs via $TS(H^+DKP\{N^1\sim CO^2\sim C\}) \text{ or } TS(H^+DKP\{N^2\sim CO^1\sim C\}), \text{ respectively, resulting in two } C_6H_{11}N_2O^+CO^+CO^-C^-C^-\})$ isomers ($[a_2]^+$, the same structure as that formed from AMPOx⁺, and $[a_2]^{+*}$), Figure 5 and Scheme 2. Because the rate-limiting TSs for [a₂]⁺ formation from H⁺DKP are higher in energy than that from AMPOx⁺ (by 44 – 68 kJ mol⁻¹), the calculations also indicate that little (MP2) or no (B3LYP) energy is required for further decarbonylation of $[a_2]^+$ and $[a_2]^{+*}$, although B3P86 suggests 39 – 52 kJ $mol^{\text{-}1}$ is required. This second decarbonylation forms the competing $H^{\text{+}}(pyr)$ and $[a_1]^{\text{+}}$ product ions, regardless of which amide is initially protonated. Thus, the $[a_2]^+$ product should be more difficult to observe in the H⁺DKP case according to B3LYP and MP2 calculations. Compared to the situation for AMPOx⁺, one can conclude that the absence of a large $[a_2]^+$ cross section would indicate that little or no Oxa precursor is likely present. Indeed, Armentrout and Clark showed that the Oxa [b₂]⁺ ion from H⁺GGG decomposes to form a large [a₂]⁺ product cross section, whereas the isomeric H⁺DKP structure also generates [a₂]⁺ but with a cross section smaller by about an order of magnitude [26]. They also observed ketenes from H⁺DKP decomposition [26], which are not observed in the present study. As such, the absence of ketenes in Figures 1 and 2 further validates that H⁺DKP is not produced in this study.

Decarbonylation and Imine Loss from $[a_2]^+$

As alluded to above, further decomposition of the $[a_2]^+$ product involves another decarbonylation reaction followed by competitive separation of the resulting fragments, here $H^+(pyr) + CH_2NH$ and $[a_1]^+ + pyr$. The $[a_2]^+$ fragment from AMPOx⁺ decarbonylates via $TS([a_2]^+\{N^2\sim CO^1\sim C\})$, Figure 4, lying 306-391 kJ mol⁻¹ above the GS, Table 1. This process forms a proton bound complex of CO, CH_2NH , and pyrroline. Loss of CO occurs easily as it requires only 7-13 kJ mol⁻¹. Calculations indicate that the $[a_2-CO]^+$ intermediate will not be observed because the TS lies above channels for further decomposition of the $[a_2-CO]^+$ intermediate into the $H^+(pyr)$ and $[a_1]^+$ fragments. The proton affinity of CO has been measured as

594 \pm 3 kJ mol⁻¹ and that of CH₂NH is 853 \pm 8 kJ mol⁻¹ [62]. Cappa and Elrod calculated a theoretical proton affinity of 1-pyrroline as 926 kJ mol⁻¹ using a variation of G2 theory previously shown to provide proton affinities that deviate from experimental measurements by less than 10 kJ mol⁻¹ [63, 64]. (Here, these proton affinities have been calculated as 581 – 594, 859 – 868, and 922 – 939 kJ mol⁻¹, respectively.) As a result, H⁺(pyr) is the dominant product formed and is limited by TS([a₂]⁺{N²~CO¹~C}), whereas [a₁]⁺ is limited by a PSL TS. Theoretical calculations predict thresholds for these two product channels of 146 – 219 and 189 – 276 kJ mol⁻¹, respectively, when coming from the AMPOx⁺ [b₂]⁺ reactant (306 – 391 and 349 – 449 kJ mol⁻¹ relative to the H⁺GPA GS, Table 1). Decomposition of H⁺DKP forms either [a₂]⁺ or [a₂]^{+*}, where the latter lies 44 – 50 kJ mol⁻¹ higher in energy. Their TSs for decarbonylation are similar in energy with that for [a₂]^{+*} lying 3 – 11 kJ mol⁻¹ higher in energy, Table 2. As shown in Scheme 2, both pathways yield the same proton bound complex of (CH₂NH)H⁺(pyr).

$[y_2 + 2H]^+/[a_1]^+$ Formation

The formation of $[y_2 + 2H]^+$ and $[a_1]^+$ product ions from protonated tripeptides has been studied by Aribi et al.,⁵⁹ Klassen and Kebarle [61], Paiz and Suhai [23], and our group [15, 16]. For H⁺GPA, we deduce reaction pathways that parallel these previous studies. Detailed reaction mechanisms for the formation of $[y_2 + 2H]^+$ and $[a_1]^+$ products can be found in Supplementary Figure S5. As described above for $[b_2]^+$ formation, the GS must first rearrange and undergo *cis/trans* isomerization to form $[N^1]$ -gtgttgtt. Next, formation of the $[y_2 + 2H]^+$ and $[a_1]^+$ products is accomplished by directly transferring the proton from N^1 to N^2 . This is followed by decarbonylation through TS(H⁺GPA[N²]-gtgttgtt{N¹C~CO¹~N²C}), Figure 4, lying 164 – 197 kJ mol⁻¹ above the GS according to theoretical calculations, Table 1. The resulting structure is a proton-bound complex of CH₂NH, ProAla (PA), and CO. Loss of CO from the complex requires only 25 – 28 kJ mol⁻¹ such that a (CH₂NH)H⁺(PA) product is readily formed. This species was not observed experimentally because the energy of the $[y_2 + 2H]^+$ CH₂NH + CO products lies below that for TS(H⁺GPA[N²]-gtgttgtt{N¹C~CO¹~N²C}) by 4 – 25 kJ mol⁻¹, Table 1, such that this TS is rate-limiting for $[y_2 + 2H]^+$ formation. Because this tight TS is disfavored entropically,

formation of $[y_2 + 2H]^+$ is disfavored compared with $[b_2]^+$ formation, Figure 1. Once the $(CH_2NH)H^+(PA)$ complex is formed, the proton affinity of each fragment dictates the probability of product formation. The proton affinity of CH_2NH is 853 ± 8 kJ mol⁻¹ [62], whereas that for PA is calculated as 963 kJ mol⁻¹ at the B3LYP/6-31G(d) level of theory [65]. These values agree reasonably well with the present calculations, which provide proton affinities for CH_2NH and PA of 859 - 868 and 982 - 993 kJ mol⁻¹, respectively. Thus, the product having the highest proton affinity is observed to have the lowest threshold, H^+PA ($[y_2 + 2H]^+$), with $CH_2NH_2^+$ ($[a_1]^+$) observed at higher energies (by 123 - 126 kJ mol⁻¹ according to theory), and H^+CO not competing, Figure 1.

In the H⁺GGG and H⁺GAG systems, the (CH₂NH)H⁺(PA) intermediate was also observed to deamidate, yielding the overall loss of CO + NH₃. ¹⁵⁻¹⁶ The analogous product, CH₂PA⁺ shown in Scheme 1, was not observed in the present study. Details regarding why this is the case can be found in the Supplementary Data but are associated with the observation that the TS leading to deamidation, TS(H⁺GPA-CO[N²-N¹]), Figure 4, lies close in energy to the initial decarbonylation TS, TS(H⁺GPA[N²]-gtgttgtt{N¹C~CO¹~N²C}), Table 1, such that this entropically disfavored process cannot compete with formation of [$y_2 + 2H$]⁺ + PA. In contrast, for H⁺GGG and H⁺GAG, the deamidation step is much lower in energy such that this process is enthalpically favored. *Decomposition of* [$y_2 + 2H$]⁺

Decomposition of the $[y_2 + 2H]^+$ product is another possible pathway for formation of $[y_1 + 2H]^+$, as previously observed for both H⁺GGG and H⁺GAG at higher energies [15, 16]. This reaction involves moving the proton in H⁺PA from N² to N³ followed by decarbonylation (loss of CO²) over TS($[y_2 + 2H]^+[N^3]$ -cggtt{ $C\sim CO^2\sim N^3$ }), Figure 4. This process forms a proton bound complex of pyr and Ala that is not observed because theory indicates little or no energy is required to dissociate to H⁺(pyr) + Ala, reaction (6a). The decarbonylation TS lies -4 – 24 kJ mol⁻¹ above the H⁺(pyr) + Ala product asymptote, whereas it lies 12 - 37 kJ mol⁻¹ below the $[y_1 + 2H]^+$ (H⁺Ala) product asymptote. Thus, the former product is observed, Figure 1, and as noted above, this process explains the decline in the $[y_2 + 2H]^+$ product at higher energies and the larger magnitude of

 $H^+(pyr)$ in Figure 1 compared to Figure 2. The observation of $H^+(pyr)$ is consistent with the relative proton affinities of C_4H_7N and Ala, 926 kJ mol⁻¹ [63, 64] versus 894.5 \pm 0.4 kJ mol⁻¹ (measured by Bouchoux and Salpin via the thermokinetic method) [66]. Present calculations indicate proton affinities of 935 – 958 and 894 – 906 kJ mol⁻¹, respectively. Failure to observe the H^+ Ala product is probably a consequence of its lower proton affinity coupled with the fact that the proton resides on the pyrroline fragment during the decarbonylation step, such that formation of H^+ Ala is also disfavored entropically.

$[b_3]^+$ Formation (Loss of Water from H^+GPA)

Detailed mechanisms for peptide dehydration reactions have previously been studied for systems including H⁺GGG [15, 67, 68], H⁺GAG [16], H⁺AGG [69], various dipeptides [24, 34, 70-72], and leucine-enkephalin [73]. As seen with H⁺GGG [15] and H⁺GAG [16], H⁺GPA likely loses water from the C-terminus. Briefly, theoretical calculations indicate that the C-terminus rotates to have its O⁴H group in close proximity to the protonated N-terminus. Proton transfer to O⁴ occurs through the tight TS(H⁺GPA[N¹-O⁴]-(gt)cgttcgt{C \sim O⁴H}), Figure 4, lying 144 – 148 kJ mol⁻¹ above the GS, Table 1. A water molecule detaches as O² attacks the carbon of the C-terminus and creates an Oxa structure, protonated 1-glycyl-2-pyrrolo-4-methyl oxazolone (H⁺GPMOx[N³]), with products lying 112 – 130 kJ mol⁻¹ above the GS and 14 – 36 kJ mol⁻¹ below the TS. The detailed mechanism can be seen in Supplementary Figure S6. Overall, [b₃]⁺ product formation is limited by the tight TS(H⁺GPA[N¹-O⁴]-(gt)cgttcgt{C \sim O⁴H}) and therefore is entropically less favored than [b₂]⁺, accounting for its small cross section in Figure 1, even though the energy of its TS is *below* that for [b₂]⁺ formation by 12 – 65 kJ mol⁻¹, Table 1.

 $TS(H^+GPA[N^1-O^4]-(gt)cgttcgt\{C\sim O^4H\})$ is similar to the TSs determined for the dissociation of H^+GGG [15] and H^+GAG [16] into $[b_3]^+$ products. However, for H^+GPA , the proton is transferred directly from N^1 to O^4 as opposed to transfer via O^1 . As mentioned above, the proline peptide favors a *cis* configuration that promotes the protonation of the N-terminus as it is charge-stabilized by surrounding oxygen atoms. Thus, it is facile for the C-terminus to rotate in the H^+GPA GS to put the O^4H in close proximity to the N-terminus for a direct $[N^1-O^4]$ proton transfer. In the

case of H⁺GGG and H⁺GAG, the GSs favor *trans* configurations for their first peptide bond with O^1 protonated. This charge is stabilized by a charge-dipole interaction with O^2 while the C-terminus is extended away from the protonation site. As a result, not only must the C-terminus move closer for protonation, but the first peptide bond must also be rotated away from the protonation site to allow the tight $TS(H^+GXG[O^1-O^4])$. The H⁺GGG study also investigated proton transfer from the N-terminus but found it to be higher in energy than that coming from O^1 [15]. *Decarbonylation of* $[b_3]^+$ to $[a_3]^+$ and Further Decomposition

Previous work has studied formation of [a₃]⁺ products by sequential decarbonylation of the Oxa [b₃]⁺ products [15, 16, 74, 75], similar to the [b₃]⁺ H⁺GMPOx precursor here. For H⁺GGG, the lowest energy pathways calculated for [a₃]⁺ product formation retained the water on the resulting [b₃]⁺ product; however, water loss required less energy than [a₃]⁺ formation in the presence of water [15]. As a result, decarbonylation of the [b₃]⁺ Oxa structure likely occurs in the absence of water, as demonstrated by rate constant calculations and better correspondence with theoretical energies [15]. Similar reasoning should be operative in the H⁺GPA system.

The mechanisms for [b₃]⁺ formation and [a₃]⁺ formation in the absence of water from H⁺GPA parallel those identified for H⁺GGG [15] across all levels of theories. A complete reaction potential energy surface for this process can be found in Supplementary Figure S6. This shows that [a₃]⁺ formation was calculated to be limited by TS(H⁺GPMOx[N³]-gtggtt{C~CO³}), Figure 4, lying 228 – 256 kJ mol⁻¹ above the H⁺GPA GS, Table 1. This TS leads to formation of [a₃]⁺ + H₂O + CO lying 148 – 195 kJ mol⁻¹ above the GS and 61 – 80 kJ mol⁻¹ below the TS. We also investigated the possibility that the [a₃]⁺ cross section is particularly small because [a₃]⁺ decomposes, a suggestion of Allen et al. [76]. As described more fully in the Supporting Data, decomposition of [a₃]⁺ to [b₂]⁺ requires only 28 – 71 kJ mol⁻¹ above the rate-limiting step for [a₃]⁺ formation. Thus, this facile decomposition along with the small cross section of its [b₃]⁺ precursor explains the low intensity of the [a₃]⁺ cross section.

$[a_1]^+$ Formation

As noted in the sections above, there are multiple pathways for formation of CH₂NH₂⁺, the

[a_1]⁺ product. In reaction (7a), [a_1]⁺ formation competes directly with reaction (3) forming H⁺PA [$y_2 + 2H$]⁺ with a mechanism outlined above. Reactions (7b) and (7c) correspond to the sequential dissociation of the [a_2]⁺ product formed in reactions (5a) and (5b), respectively. In both cases, [a_1]⁺ formation competes with C₄H₇NH⁺ (H⁺(pyr)) formation, as detailed above. For all three processes, the product asymptote is the rate-limiting step along the reaction pathway. Reaction (7a) represents the lowest energy pathway for [a_1]⁺ formation, lying 265 – 315 above the H⁺GPA GS, Table 1. *Analysis of Primary and Secondary Dissociation Channels of H*⁺*GPA*

All of the degradation reactions in this study are outlined in Scheme 1. The primary decomposition products from H⁺GPA include the $[b_2]^+$ AMPOx⁺ structure from loss of Ala in reaction (4a), the $[b_3]^+$ H⁺GPMOx structure from dehydration of the C-terminus in reaction (1), the $[y_2 + 2H]^+$ H⁺PA structure resulting from loss of CO rapidly followed by imine loss in reaction (3), and the $[a_1]^+$ iminium structure formed in reaction (7a). Formation of the $[b_2]^+$ Oxa structure is limited by its asymptotic product energy, whereas the formations of $[b_3]^+$ and $[y_2 + 2H]^+$ are limited by tight TSs, TS(H⁺GPA[N¹-O⁴]-(gt)cgttcgt{C \sim O⁴H}) and TS(H⁺GPA[N²]-gtgttgtt {N¹C \sim CO¹ \sim N²C}), respectively. Note that the initial loss of CO requires an amount of energy that already exceeds that needed for further decomposition into the $[y_2 + 2H]^+$ product, such that the decarbonylation product (CH₂NH)H⁺PA at m/z 216 is not observed. This initial decarbonylation can also lead to the formation of $[a_1]^+$; however, unlike $[y_2 + 2H]^+$ formation, formation of $[a_1]^+$ is limited by the asymptotic energy of its products, calculated to lie 101 – 121 kJ mol⁻¹ higher than the TS(H⁺GPA[N²]-gtgttgtt{N¹C \sim CO¹ \sim N²C}), Table 1.

The analysis of the cross sections for these four primary processes involved extrapolating them to zero-pressure conditions yielding rigorous single-collision conditions between the reactant ion and the Xe gas. Such conditions are required in order to accurately quantify the amount of energy available for decomposition. Next, the total cross section was modeled using the TS for the $[b_2]^+$ product, the dominant product throughout the threshold region. This established a value for the n parameter in Supplementary Eq. (S1) that controls the shape of the cross sections for all products. Then, cross sections of any sequential product channels were summed with the channels

of their respective precursor ions in order to form composites. Specifically, m/z 127 and 70 were summed with m/z 155 ($[b_2]^+ + [a_2]^+ + H^+(pyr) = [b_2]^+_{tot}$), and m/z 226 was summed with m/z 198 ($[b_3]^+ + [a_3]^+ = [b_3]^+_{tot}$). Then, Supplementary Eq. (S1) was used to model $[b_2]^+_{tot}$, $[b_3]^+_{tot}$, $[y_2 + 2H]^+$, and $[a_1]^+$. In order to reproduce the relative magnitudes accurately, vibrational frequencies below 900 cm⁻¹ of the rate-limiting TSs for the $[b_3]^+_{tot}$ and $[y_2 + 2H]^+$ channels were scaled by 0.825 and 0.75, respectively, indicating that these tight TSs are somewhat looser than originally calculated. (Here, it is useful to note that the output of the Gaussian program warns that thermodynamic functions may be in error for vibrational frequencies under 900 cm⁻¹, in large measure because such vibrations may no longer be treated accurately as harmonic at temperatures of interest. Past work indicates that differences between computed and experimental force constants are systematic such that generalized scaling procedure to bring computed vibrational spectra into agreement with experimental data is justified [77]. This procedure was first recognized in our evaluation of H⁺Asn [78] and has also proven to be effective for the H⁺GGG [15] and H⁺GAG [16] systems, as well as many others.) This procedure yielded 0 K energy thresholds for the primary product channels and the other modeling parameters listed in Table 3.

It is important to note that the $[y_2 + 2H]^+$ and $[a_1]^+$ cross sections are treated as primary products even though they result from initial CO loss (forming an unobserved intermediate) followed by separation of the resultant ions into the competing product channels, according to theory. Here, the $[y_2 + 2H]^+$ cross section can be modeled unambiguously with the rate-limiting TS for CO loss, $TS(H^+GPA[N^2]-gtgttgtt\{N^1C\sim CO^1\sim N^2C\})$. The main challenge in modeling $[a_1]^+$ product formation stems from its rate-limiting PSL where one ionic and two neutral fragments are generated. Our modeling of such channels requires that a single neutral is formed [44], such that we associate the CO and ProAla products as a single neutral complex. More details on this procedure can be found in the Supplementary Data, but previous tripeptide studies from our group suggest this approach produces reasonable results [15, 16]. In the present case, it can be realized that this approach affects the rovibrational frequencies and the polarizability of the neutral molecule needed for the modeling. This approximation should result in a tighter TS than for three

separate products, such that the kinetic shift might be overestimated. Thus, the true threshold may lie at higher energies, such that this value might be considered a lower limit. The multiple pathways available to formation of $[a_1]^+$ may also have influenced the modeling of this channel.

Once the four primary channels were modeled, the sequential product channels could be modeled one channel at a time, such that competition with all other primary channels was included. The secondary channels include $[a_2]^+_{tot} = [a_2]^+ + H^+(pyr)$ (from $[b_2]^+$) and $[a_3]^+$ (from $[b_3]^+$). More details on this procedure can be found in the Supplementary Data. Here, we note that because the $[a_3]^+$ product channel could not be collected reliably at low pressures, a high pressure data set was modeled. Then, corrections for the pressure dependence of this channel were made. Furthermore, decomposition of the $[a_3]^+$ fragment could not be reliably investigated.

Figure 6 shows the model for the four primary channels along with sequential dissociation of $[b_2]^+$ to $[a_2]^+$ with parameters used listed in Table 3. The resulting model accurately reproduces the $[b_2]^+$, $[a_2]^+$, $[y_2 + 2H]^+$, $[a_1]^+$, and $[b_3]^+$ cross sections from threshold through ~ 5 eV. The discrepancies at higher energies can occur because additional processes not included in the modeling become active. Table 3 shows that the $[b_3]^+$ ion has the lowest threshold with those for $[b_2]^+$ and $[y_2 + 2H]^+$ nearly equal and higher. This contrasts with the apparent thresholds seen in the figure, where the differences occur because the tight TSs for $[b_3]^+$ and $[y_2 + 2H]^+$ lead to much larger kinetic shifts than for the $[b_2]^+$ product, which is limited by a loose PSL TS. The other primary product, $[a_1]^+$, also has a measured threshold that is much lower than its apparent threshold even though it is also limited by a PSL TS; however, this channel is inhibited by competition with the lower energy channels.

The $[a_2]^+$ product is the result of decarbonylation of AMPOx⁺ $[b_2]^+$, which is limited by the tight TS(AMPOx⁺{C~CO²~O¹}). As shown in Figure 6, modeling the $[a_2]^+$ cross section in this fashion reproduces this channel nicely as well as capturing some of the decline in the $[b_2]^+$ cross section. As shown in Supplementary Figure S7, the same can be said for modeling the $[a_3]^+$ product cross section as a sequential product from the $[b_3]^+$ fragment and limited by the tight TS(H⁺GPMOx[N³]-gtggtt{C~CO³}).

Analysis of Primary and Secondary Channels of AMPOx⁺ [b₂]⁺

Our modeling program, CRUNCH, is not designed to model tertiary channels directly; [46] however, by generating the $[b_2]^+$ primary product in the source [33], we can model the formation of $[a_2]^+$, $H^+(pyr)$, and $[a_1]^+$ products formed by decomposition of $[b_2]^+$ ions, where the latter two are tertiary products of H⁺GPA, Figure 2. The initial decarbonylation of $[b_2]^+$ is limited by the tight TS(AMPOx⁺{C~CO²~O¹}), and the latter two reaction pathways both go through an unobserved intermediate, $[a_2 - CO]^+$. Here, formation of $H^+(pyr) + CH_2NH + CO$ is straightforwardly modeled because it is limited by the tight $TS([a_2]^+\{N^2\sim CO^1\sim C\})$, but because formation of the competing [a₁]⁺ + C₄H₇N +CO channel is limited by a PSL TS, the neutral product in this reaction was treated as CO hydrogen bound to 1-pyrroline. The models use parameters listed in Table 3 and are shown in Figure 2. Clearly, the data are modeled well through ~3.5 eV, but at higher energies, the decline in the $[a_2]^+$ cross section is not reproduced. We believe this may be a result of limitations in the assumptions needed for the sequential model, which assumes that the internal and translational energies of the primary products (ion and neutral) are characterized by a statistical distribution with the zero of energy for the product at its threshold, an assumption that is appropriate for loose TSs [46]. In the present system, formation of the primary $[a_2]^+$ + CO products is limited by $TS(AMPOx^{+}\{C\sim CO^{2}\sim O^{1}\})$, Supplementary Figure S3. This tight TS is calculated to lie 107-126kJ mol⁻¹ above the resulting (CO)(CH₂NH)H⁺(pyr) complex and 99 – 113 kJ mol⁻¹ above the separated CO + (CH₂NH)H⁺(pyr) products that then lead to the final H⁺(pyr) + CH₂NH and $[a_1]$ ⁺ + pyr products. The energy of this reverse activation barrier can be released to the (CH₂NH)H⁺(pyr) + CO products in a non-statistical (and unknown) fashion that depends on the details of the potential energy surface. Further, no matter how the energy is released, the complex actually lies in a deeper potential well (here by $\sim 106 \pm 7 \text{ kJ mol}^{-1}$) than the sequential model assumes. According to RRKM theory, this increases the density of states of the complex, which reduces that rate constant for further dissociation. The result is a larger kinetic shift that shifts thresholds for further decomposition up in energy. As a consequence, these sequential thresholds should be considered as upper limits. This conclusion can be checked by comparison to theory, see below.

The quality of the resulting thermochemistry can be checked in this case by comparing the threshold energies for formation of $[a_2]^+$ coming from H⁺GPA and $[b_2]^+$ AMPOx⁺. The sequential model for reaction (5a), $H^+GPA \rightarrow [a_2]^+ + A + CO$, has a threshold of 3.25 ± 0.10 eV, which can be compared to the value obtained by adding the threshold measured for reaction (4a), H⁺GPA → $[b_2]^+ + A$, 2.16 ± 0.05 eV to that for the directly measured $[b_2]^+ \rightarrow [a_2]^+ + CO$, 1.24 ± 0.14 eV. The sum of 3.40 ± 0.14 eV agrees well with the sequential threshold, verifying that the $[a_2]^+$ product is formed from $[b_2]^+$ AMPOx⁺ fragmentation. In contrast, formation of $[a_1]^+$ in reaction (7b), i.e., through $[b_2]^+$ and $[a_2]^+$, should have a threshold of $(2.16 \pm 0.05) + (<2.90 \pm 0.16) = <5.06 \pm 0.17$ eV, which is well above that measured for reaction (7a), 3.06 ± 0.07 eV. (Theory indicates that reaction (7b) does not begin until 0.87 - 1.39 eV above reaction (7a).) This shows that the formation of $[a_1]^+$ from H⁺GPA does indeed follow reaction (7a) at threshold, and $[b_2]^+$ decomposition is probably a minor contributor. Because it is a tertiary product, the threshold for formation of H⁺(pyr) in reaction (6a) could not be determined, but the sum of the threshold energies measured for $[b_2]^+$ in reaction (4a) (2.16 \pm 0.05 eV) with that for H⁺(pyr) from AMPOx⁺ (<2.58 ± 0.16 eV) indicates that reaction (6a) should have a threshold of <4.74 \pm 0.17 eV. This value is in reasonable agreement with the apparent threshold of Figure 1 once pressure effects and the energy distributions are taken into account.

Discussion

Comparison between Theoretical and Experimental Energies

Although reproduction of the data is one metric for evaluating the veracity of the mechanisms and their energetics, comparison of the theoretical and experimental energies should also provide confidence that the correct thermochemistry has been extracted and correct mechanisms and product structures identified. These values are compared in Table 4 and Figure 7. For the thresholds associated with H⁺GPA decomposition, it can be seen that B3LYP systematically underestimates the threshold energies. The thresholds measured for $[b_2]^+$, $[y_2 + 2H]^+$, $[a_2]^+$, and $[a_3]^+$ agree best with the MP2 level of theory, whereas all three levels are in

reasonable agreement with the [b₃]⁺ threshold. Because the [a₁]⁺ threshold may be a lower limit, both B3P86 and MP2 provide reasonable values. The mean absolute deviations (MADs) between theory and experimental results for H⁺GPA decomposition are on average smallest when using the MP2 level of theory (6 kJ mol⁻¹), whereas the deviations are on average highest when using the B3LYP level of theory (15 kJ mol⁻¹).

As noted above, certain approximations had to be made for some of the fragments, which may affect the reported experimental threshold energies. Both the $[y_2 + 2H]^+$ and $[a_1]^+$ channels are thought to go through an unobserved intermediate, such that the $[a_1]^+$ fragment had to be modeled as a PSL TS with the composite PA•CO neutral product, leading to the lower limit listed in Table 4. The $[a_3]^+$ channel could not reliably be collected at low pressures, such that our method for accounting for the pressure effects in this channel may have introduced error in determining this threshold value. Our extrapolation assumed that all channels have the same pressure dependence, which is reasonable but not explicitly correct. Hence, we averaged the pressure dependences of the other channels as an approximation of the pressure dependence of the $[a_3]^+$ channel.

For decomposition of AMPOx⁺ [b₂]⁺, all three levels of theory are in reasonable agreement with the measured threshold for production of $[a_2]^+$. In contrast, the H⁺(pyr) and $[a_1]^+$ threshold energies are underestimated across all levels of theory. As noted above, the analysis of these channels is adversely affected by the statistical assumptions intrinsic in the sequential model [46], such that these experimental values are best viewed as upper limits. However, the difference in these experimental threshold energies (31 \pm 4 kJ mol⁻¹) is in reasonable agreement with the differences predicted by B3LYP (43 kJ mol⁻¹) and MP2 (44 kJ mol⁻¹) theory.

Cis Versus Trans Reactant

As discussed in the introduction, other investigators have observed the kinetic trapping of *trans* isomers of proline peptide bonds [27, 58]. If such isomers were present in abundance in the current experiments, then the measured thresholds would correspond to the higher energy *trans*-Pro isomer [N¹]-gtgttgtt, rather than the [N¹]-tcgctgtt GS, Figure 3. We investigated this possibility by modeling the $[b_2]^+$ data assuming an $[N^1]$ -gtgttgtt reactant and comparing the resulting threshold

with theoretical calculations. The experimental threshold changes only slightly, to 208 ± 5 kJ/mol, whereas theory indicates that the $[b_2]^+$ threshold from the *trans*-Pro conformer is 122, 134, and 178 kJ mol⁻¹ for the B3LYP, B3P86, and MP2 levels of theory, respectively. These deviations are far greater than those for the *cis*-Pro conformer, Table 4. We can also consider what the results might look like if the *trans*-Pro conformer were present as a minor contributor to the reactant ion beam. In such a case, we should observe a low-energy feature on all the cross sections, which should be relatively distinct given the 31 - 39 kJ mol⁻¹ (0.32 – 0.41 eV) difference calculated between the two conformers, Figure 3. No such feature is observed in any of the reaction products, including $[b_2]^+$ where the sensitivity should be greatest (about 1%). As a result, our experimental results are most consistent with only the *cis*-Pro conformer being present as a reactant.

Influence from the Proline Effect

The present work further elucidates how the proline residue affects the formation of the Oxa structure. Urban and Vaisar suggested that $[b_2]^+$ product formation is hindered by the extra ring strain caused by the proline residue [20], whereas Grewal et al. suggested that this effect is either negligible or minor [21]. These two conclusions may be system dependent. Grewal et al. identified a tight rate-limiting TS for Oxa formed from H⁺GPG, TS(H⁺GPG[N²]{CO²~N²}) (using the present nomenclature), whereas the present study identifies a rate-limiting PSL TS. In the latter case, any energy from ring strain directly contributes to the total energy of the final Oxa products and thus directly to its threshold for formation. In contrast, when $[b_2]^+$ formation is limited by a tight TS, the ring strain energy need not influence the height of the barrier. Grewal calculated the ring strain energy as being fairly minor (10.9 kJ mol⁻¹ when Oxa is generated from H⁺GPG versus H⁺PGG [21]), but even so, when $[b_2]^+$ formation is limited by a PSL TS, then the ring strain energy may influence $[b_2]^+$ formation. Other influences of the presence of the proline residue become more apparent by comparison with the behavior of other tripeptides, as discussed in the next section.

Comparison of H⁺GPA to H⁺GGG and H⁺GAG Decomposition

In all three systems, the $[b_2]^+$ channel produces the largest cross section and is limited by a

PSL TS from which an Oxa product can decompose into the $[a_2]^+$ fragment and then undergo further decarbonylation. The threshold for $[b_2]^+$ formation is somewhat higher here, 206 ± 5 kJ mol⁻¹, than for H⁺GGG and H⁺GAG, 171 ± 6 and 160 ± 14 kJ mol⁻¹, respectively. This difference can be associated with the stabilization of the H⁺GPA ground structure provided by the *cis*-peptide bond, thereby allowing stronger hydrogen bonding. Further, the oxazolone product formed from H⁺GGG¹⁵ or H⁺GAG¹⁶ has the N² protonated, which allows a strong hydrogen bond with the N-terminus. In contrast, in AMPOx⁺, N² is a quaternary nitrogen, which still interacts with the N-terminus (Figure 4) but no longer by the hydrogen bond that stabilizes the Oxa product in the other two systems.

Unlike H⁺GGG [15] and H⁺GAG [16], H⁺GPA does not decompose to produce an observable $[a_2 - CO]^+$ cluster product. As discussed above, this is because the decarbonylation $TS([a_2]^+\{N^2\sim CO^1\sim C\})$ already contains enough energy to allow the $(CH_2NH)H^+$ (pyr) cluster to decompose to H⁺(pyr) + CH₂NH. Here, this product asymptote is relatively low in energy because the secondary nitrogen of pyr has a high proton affinity (proline effect). In the case of H⁺GGG or H⁺GAG decomposition, the $[a_2 - CO]^+$ cluster consists of $(CH_2NH)H^+$ (RCHNH) (where R = H or CH₃, respectively). Because the latter complexes are composed exclusively of primary amines, the energy for further decomposition to form H⁺RCHNH lies above the decarbonylation TS leading to $[a_2 - CO]^+$, thereby allowing observation of the product.

Similarly, the high proton affinity of the tertiary amide in a proline residue [17, 20, 79] has been linked to the high abundance of $[y_n + 2H]^+$ fragments observed in previous studies, the so-called proline effect [18-22, 27, 65]. In contrast to these expectations, H⁺GPA decomposition produces a smaller $[y_2 + 2H]^+$ cross section than H⁺GGG [15] (which has the largest $[y_2 + 2H]^+$ cross section) or H⁺GAG [16]. This result seems at odds with the observation that the thresholds for $[y_2 + 2H]^+$ formation in the latter two systems exceed that for $[b_2]^+$ by 0.88 ± 0.12 and 0.55 ± 0.32 eV, respectively, whereas the thresholds in the present study are roughly equivalent, Table 4. As noted above, the lower $[y_2 + 2H]^+$ threshold observed here can be attributed to the higher proton affinity of proline, which lowers the energy needed for initial decarbonylation as well as the final

product energy. In the H⁺GPA case, the energy of the final $[y_2 + 2H]^+ + CH_2NH + CO$ products is lowered to the point where the product is limited by the tight TS needed for decarbonylation, such that this channel is entropically disfavored compared to $[b_2]^+$ formation. In contrast, the $[y_2 + 2H]^+$ channels for H⁺GGG and H⁺GAG are limited by their products in loose PSL TSs, and therefore compete more effectively with the $[b_2]^+$ channel.

The $[a_1]^+$ cross section is smallest in the present system, consistent with it having the highest experimental threshold (295 ± 7 kJ mol⁻¹ here versus 247 ± 7 and 261 ± 17 kJ mol⁻¹ for H⁺GGG and H⁺GAG, respectively). In all three H⁺GXY systems, the threshold for $[a_1]^+$ formation is associated with the primary process that competes directly with formation of $[y_2 + 2H]^+$, H⁺XY. As noted above, H⁺PA has a lower threshold than formation of H⁺GG (from H⁺GGG) or H⁺AG (from H⁺GAG) such that formation of $[a_1]^+$ is less competitive in the present system, an indirect effect of the higher proton affinity of the proline residue.

Another notable observation is that H^+GPA decomposition yields a $[b_3]^+$ cross section that is much larger than that of H^+GGG [15] and H^+GAG [16]. Theoretical calculations suggest that this is because the proline favors a *cis* configuration, which places the protonated N-terminus in close proximity to the C-terminus, thereby allowing more facile proton transfer. Furthermore, the larger $[b_3]^+$ cross section leads to a larger $[a_3]^+$ cross section as a sequential product.

Finally, we note that in both the H^+GGG and H^+GAG systems, the loss of $CO + NH_3$ was observed, whereas a similar product is not found for H^+GPA . This possibility was explored computationally, as described in the Supporting Data. There it is shown that loss of $CO + NH_3$ is disfavored enthalpically and entropically compared to $[y_2 + 2H]^+$ and $[a_1]^+$ formation, whereas for the H^+GGG and H^+GAG systems, this channel is enthalpically more favorable.

Conclusions

The present study has examined the kinetic-energy-dependent decomposition of protonated H^+GPA and its $[b_2]^+$ fragment by collisions with Xe using GIBMS. Analysis of the CID cross sections yields 0 K threshold energies for the $[b_2]^+$, $[b_3]^+$, $[y_2 + 2H]^+$, $[a_2]^+$, $[a_3]^+$, $H^+(pyr)$, and $[a_1]^+$

product ions. Effects taken into account include lifetime effects, pressure dependence, reactant energy distributions, and competition among primary and sequential dissociation channels. Overall, the MP2 level of theory agrees well with the experimentally obtained threshold values, and there is very good agreement with at least one level of theory for all experimental thresholds. This agreement strongly suggests that the *cis*-Pro [N¹]-tegetgtt conformer is the ground structure present and that *cis/trans* isomerization is necessary, but not rate-limiting, for $[b_2]^+$ Oxa formation. This *cis* configuration appears to make protonation of the C-terminus more energetically feasible, which explains why the $[b_3]^+$ cross section is so much more prominent for H⁺GPA fragmentation compared to H⁺GGG and H⁺GAG fragmentation [15, 16]. Further, no products corresponding to $[y_1 + 2H]^+$, $[a_2 - CO]^+$, $[y_2 + 2H - CO]^+$, or combined CO + NH₃ loss are observed, which theoretical calculations indicate results from the unique geometry and proton affinity of proline. Such quantitative information is important in elucidating why proline has unique properties with regards to peptide fragmentation patterns.

Furthermore, this study describes the reaction pathways involved during $[b_2]^+$ AMPOx⁺ formation, which are confirmed by the good agreement between the experimental and theoretical threshold energies. Experimentally, the absence of an H⁺DKP product structure for $[b_2]^+$ can be deduced from the relatively low threshold for $[b_2]^+$ formation, the relatively large $[a_2]^+$ cross section, the lack of a $[y_1 + 2H]^+$ product, and the lack of ketene products. Theory supports these observations by indicating that H⁺DKP formation is disfavored enthalpically and entropically. Future studies are envisioned that will focus on systems in which a H⁺DKP $[b_2]^+$ structure is formed and will provide experimental observations and quantitative thermochemistry measurements to compare the reaction mechanisms for its formation with those of Oxa. Ultimately, future related work will hopefully provide meaningful mechanistic information regarding peptide fragmentation patterns and identify key indicators of sequence information. Such knowledge could make characterizing larger systems easier while improving the efficiency of peptide sequencing algorithms.

Acknowledgments

This work is supported by the National Science Foundation under grant CHE-1954142 along with grants of computational time allocated by the Center for High Performance Computing at the University of Utah. We also thank Dr. Christopher McNary and Samantha Walker for the development of the simulated annealing program used to help identify the GS.

Supporting Data

General experimental procedures and equations used for thermochemical analysis are provided. Details regarding the pressure dependence for the [a₃]⁺ channel and assumptions used for the analysis AMPOx⁺ decomposition are provided. Complete reaction potential energy surfaces and tables are given for key processes, including those for unobserved products.

References

- [1] J.P. Schanstra, P. Zürbig, A. Alkhalaf, A. Argiles, S.J.L. Bakker, J. Beige, H.J.G. Bilo, C. Chatzikyrkou, M. Dakna, J. Dawson, C. Delles, H. Haller, M. Haubitz, H. Husi, J. Jankowski, G. Jerums, N. Kleefstra, T. Kuznetsova, D.M. Maahs, J. Menne, W. Mullen, A. Ortiz, F. Persson, P. Rossing, P. Ruggenenti, I. Rychlik, A.L. Serra, J. Siwy, J. Snell-Bergeon, G. Spasovski, J.A. Staessen, A. Vlahou, H. Mischak, R. Vanholder, Diagnosis and Prediction of CKD Progression by Assessment of Urinary Peptides, J. Am. Soc. Nephrol., 26 (2015) 1999-2010.
- [2] M.L. Nielsen, M.M. Savitski, R.A. Zubarev, Extent of Modifications in Human Proteome Samples and Their Effect on Dynamic Range of Analysis in Shotgun Proteomics, Mol. Cell. Proteom., 5 (2006) 2384.
- [3] I.A. Papayannopoulos, The interpretation of collision-induced dissociation tandem mass spectra of peptides, Mass Spectrom. Rev., 14 (1995) 49-73.
- [4] M. Mann, M. Wilm, Error-Tolerant Identification of Peptides in Sequence Databases by Peptide Sequence Tags, Anal. Chem., 66 (1994) 4390-4399.
- [5] J.K. Eng, A.L. McCormack, J.R. Yates, An approach to correlate tandem mass spectral data of peptides with amino acid sequences in a protein database, J. Am. Soc. Mass. Spectrom., 5 (1994) 976-989.
- [6] D.N. Perkins, D.J.C. Pappin, D.M. Creasy, J.S. Cottrell, Probability-based protein identification by searching sequence databases using mass spectrometry data, Electrophoresis, 20 (1999) 3551-3567.
- [7] V. Dančík, T.A. Addona, K.R. Clauser, J.E. Vath, P.A. Pevzner, De Novo Peptide Sequencing via Tandem Mass Spectrometry, J. Comput. Biol., 6 (1999) 327-342.
- [8] E. Mørtz, P.B. O'Connor, P. Roepstorff, N.L. Kelleher, T.D. Wood, F.W. McLafferty, M. Mann, Sequence tag identification of intact proteins by matching tanden mass spectral data against sequence data bases, Proc. Natl. Acad. Sci. U.S.A., 93 (1996) 8264-8267.

- [9] I.K. Chu, C.-K. Siu, J.K.-C. Lau, W.K. Tang, X. Mu, C.K. Lai, X. Guo, X. Wang, N. Li, Y. Xia, X. Kong, H.B. Oh, V. Ryzhov, F. Tureček, A.C. Hopkinson, K.W.M. Siu, Proposed nomenclature for peptide ion fragmentation, Int. J. Mass spectrom., 390 (2015) 24-27.
 [10] B. Paizs, S. Suhai, Fragmentation pathways of protonated peptides, Mass Spectrom. Rev.,
- 24 (2005) 508-548.
 [11] M. Zenaidee, C. Lantz, T. Perkins, J. Fu, W. Jung, R.R.O. Loo, J.A. Loo, Internal
 Fragments Generated by Electron Ionization Dissociation Enhances Protein Ton-down Mass
- Fragments Generated by Electron Ionization Dissociation Enhances Protein Top-down Mass Spectrometry, ChemRxiv, Preprint (2020).
- [12] V.H. Wysocki, G. Tsaprailis, L.L. Smith, L.A. Breci, Mobile and localized protons: a framework for understanding peptide dissociation, J. Mass Spectrom., 35 (2000) 1399-1406.
- [13] O. Burlet, R.S. Orkiszewski, K.D. Ballard, S.J. Gaskell, Charge promotion of low-energy fragmentations of peptide ions, Rapid Commun. Mass Spectrom., 6 (1992) 658-662.
- [14] A.R. Dongré, J.L. Jones, Á. Somogyi, V.H. Wysocki, Influence of Peptide Composition, Gas-Phase Basicity, and Chemical Modification on Fragmentation Efficiency: Evidence for the Mobile Proton Model, J. Am. Chem. Soc., 118 (1996) 8365-8374.
- [15] A. Mookherjee, M.J. Van Stipdonk, P.B. Armentrout, Thermodynamics and Reaction Mechanisms of Decomposition of the Simplest Protonated Tripeptide, Triglycine: A Guided Ion Beam and Computational Study, J. Am. Soc. Mass. Spectrom., 28 (2017) 739-757.
- [16] A. Mookherjee, P.B. Armentrout, Thermodynamics and Reaction Mechanisms for Decomposition of a Simple Protonated Tripeptide, H⁺GAG: a Guided Ion Beam and Computational Study, J. Am. Soc. Mass Spectrom., 30 (2019) 1013-1027.
- [17] D.F. Hunt, J.R. Yates, J. Shabanowitz, S. Winston, C.R. Hauer, Protein sequencing by tandem mass spectrometry, Proc. Natl. Acad. Sci., 83 (1986) 6233-6237.
- [18] B.L. Schwartz, M.M. Bursey, Some proline substituent effects in the tandem mass spectrum of protonated pentaalanine, Biol. Mass Spectrom., 21 (1992) 92-96.
- [19] J.A. Loo, C.G. Edmonds, R.D. Smith, Tandem mass spectrometry of very large molecules. 2. Dissociation of multiply charged proline-containing proteins from electrospray ionization, Anal. Chem., 65 (1993) 425-438.
- [20] T. Vaisar, J. Urban, Probing Proline Effect in CID of Protonated Peptides, J. Mass Spectrom., 31 (1996) 1185-1187.
- [21] R.N. Grewal, H. El Aribi, A.G. Harrison, K.W.M. Siu, A.C. Hopkinson, Fragmentation of Protonated Tripeptides: The Proline Effect Revisited, J. Phys. Chem. B, 108 (2004) 4899-4908. [22] A.C. Gucinski, J. Chamot-Rooke, V. Steinmetz, Á. Somogyi, V.H. Wysocki, Influence of
- N-terminal Residue Composition on the Structure of Proline-Containing b₂⁺ Ions, J. Phys. Chem. A, 117 (2013) 1291-1298.
- [23] B. Paizs, S. Suhai, Combined quantum chemical and RRKM modeling of the main fragmentation pathways of protonated GGG. II. Formation of b₂, y₁, and y₂ ions, Rapid Commun. Mass Spectrom., 16 (2002) 375-389.
- [24] P.B. Armentrout, A.L. Heaton, Thermodynamics and Mechanisms of Protonated Diglycine Decomposition: A Computational Study, J. Am. Soc. Mass. Spectrom., 23 (2012) 621-631.
- [25] B. Paizs, S. Suhai, Combined quantum chemical and RRKM modeling of the main fragmentation pathways of protonated GGG. I. Cis-trans isomerization around protonated amide bonds, Rapid Commun. Mass Spectrom., 15 (2001) 2307-2323.
- [26] P.B. Armentrout, A.A. Clark, The simplest b_2^+ ion: Determining its structure from its energetics by a direct comparison of the threshold collision-induced dissociation of protonated oxazolone and diketopiperazine, Int. J. Mass spectrom., 316-318 (2012) 182-191.

- [27] A. Masson, M.Z. Kamrath, M.A.S. Perez, M.S. Glover, U. Rothlisberger, D.E. Clemmer, T.R. Rizzo, Infrared Spectroscopy of Mobility-Selected H⁺-Gly-Pro-Gly-Gly (GPGG), J. Am. Soc. Mass. Spectrom., 26 (2015) 1444-1454.
- [28] K.M. Ervin, P.B. Armentrout, Translational energy dependence of $Ar^++XY \rightarrow ArX^++Y$ (XY=H₂,D₂,HD) from thermal to 30 eV c.m., J. Chem. Phys., 83 (1985) 166-189.
- [29] F. Muntean, P.B. Armentrout, Guided ion beam study of collision-induced dissociation dynamics: integral and differential cross sections, J. Chem. Phys., 115 (2001) 1213-1228.
- [30] P.B. Armentrout, Mass spectrometry—not just a structural tool: the use of guided ion beam tandem mass spectrometry to determine thermochemistry, J. Am. Soc. Mass. Spectrom., 13 (2002) 419-434.
- [31] R.M. Moision, P.B. Armentrout, An electrospray ionization source for thermochemical investigation with the guided ion beam mass spectrometer, J. Am. Soc. Mass. Spectrom., 18 (2007) 1124-1134.
- [32] T. Kim, A.V. Tolmachev, R. Harkewicz, D.C. Prior, G. Anderson, H.R. Udseth, R.D. Smith, T.H. Bailey, S. Rakov, J.H. Futrell, Design and Implementation of a New Electrodynamic Ion Funnel, Anal. Chem., 72 (2000) 2247-2255.
- [33] D.R. Carl, R.M. Moision, P.B. Armentrout, In-source fragmentation technique for the production of thermalized ions, J. Am. Soc. Mass. Spectrom., 20 (2009) 2312-2317.
- [34] P.B. Armentrout, A.L. Heaton, Thermodynamics and Mechanisms of Protonated Diglycine Decomposition: A Guided Ion Beam Study, J. Am. Soc. Mass. Spectrom., 23 (2012) 632-643.
- [35] D.R. Carl, R.M. Moision, P.B. Armentrout, Binding energies for the inner hydration shells of Ca²⁺: An experimental and theoretical investigation of Ca²⁺(H₂O)_x complexes (x=5–9), Int. J. Mass spectrom., 265 (2007) 308-325.
- [36] A.L. Heaton, R.M. Moision, P.B. Armentrout, Experimental and Theoretical Studies of Sodium Cation Interactions with the Acidic Amino Acids and Their Amide Derivatives, J. Phys. Chem. A, 112 (2008) 3319-3327.
- [37] A.L. Heaton, P.B. Armentrout, Experimental and Theoretical Studies of Potassium Cation Interactions with the Acidic Amino Acids and Their Amide Derivatives, J. Phys. Chem. B, 112 (2008) 12056-12065.
- [38] S.J. Ye, P.B. Armentrout, Absolute Thermodynamic Measurements of Alkali Metal Cation Interactions with a Simple Dipeptide and Tripeptide, J. Phys. Chem. A, 112 (2008) 3587-3596.
- [39] S.J. Ye, A.A. Clark, P.B. Armentrout, Experimental and Theoretical Investigation of Alkali Metal Cation Interactions with Hydroxyl Side-Chain Amino Acids, J. Phys. Chem. B, 112 (2008) 10291-10302.
- [40] D.R. Carl, B.K. Chatterjee, P.B. Armentrout, Threshold collision-induced dissociation of $Sr^{2+}(H_2O)_x$ complexes (x=1-6): An experimental and theoretical investigation of the complete inner shell hydration energies of Sr^{2+} , J. Chem. Phys., 132 (2010) 044303.
- [41] E. Teloy, D. Gerlich, Integral cross sections for ion—molecule reactions. I. The guided beam technique, Chem. Phys., 4 (1974) 417-427.
- [42] D. Gerlich, Inhomogeneous RF Fields: A Versatile Tool for the Study of Processes with Slow Ions, in: Adv. Chem. Phys., 1992, pp. 1-176.
- [43] N.R. Daly, Scintillation Type Mass Spectrometer Ion Detector, Rev. Sci. Instrum., 31 (1960) 264-267.
- [44] M.T. Rodgers, K.M. Ervin, P.B. Armentrout, Statistical modeling of collision-induced dissociation thresholds, J. Chem. Phys., 106 (1997) 4499-4508.

- [45] M.T. Rodgers, P.B. Armentrout, Statistical modeling of competitive threshold collision-induced dissociation, J. Chem. Phys., 109 (1998) 1787-1800.
- [46] P.B. Armentrout, Statistical modeling of sequential collision-induced dissociation thresholds, J. Chem. Phys., 126 (2007) 234302.
- [47] R.G. Gilbert, S.C. Smith, Theory of unimolecular and recombination reactions, Blackwell Scientific, London, 1990.
- [48] P.J. Robinson, K.A. Holbrook, Unimolecular reactions, Wiley Interscience, New York, 1972.
- [49] F.A. Khan, D.E. Clemmer, R.H. Schultz, P.B. Armentrout, Sequential bond energies of chromium carbonyls ($Cr(CO)_x^+$, x = 1-6), J. Phys. Chem., 97 (1993) 7978-7987.
- [50] J.E. Carpenter, C.P. McNary, A. Furin, A.F. Sweeney, P.B. Armentrout, How Hot are Your Ions Really? A Threshold Collision-Induced Dissociation Study of Substituted Benzylpyridinium "Thermometer" Ions, J. Am. Soc. Mass. Spectrom., 28 (2017) 1876-1888.
- [51] N.F. Dalleska, K. Honma, P.B. Armentrout, Stepwise solvation enthalpies of protonated water clusters: collision-induced dissociation as an alternative to equilibrium studies, J. Am. Chem. Soc., 115 (1993) 12125-12131.
- [52] C. Lee, W. Yang, R.G. Parr, Development of the Colle-Salvetti correlation-energy formula into a functional of the electron density, Phys. Rev. B, 37 (1988) 785-789.
- [53] W.J. Hehre, Ab initio molecular orbital theory, Acc. Chem. Res., 9 (1976) 399-406.
- [54] A.D. Becke, Density-functional thermochemistry. III. The role of exact exchange, J. Chem. Phys., 98 (1993) 5648-5652.
- [55] H.B. Schlegel, Optimization of equilibrium geometries and transition structures, J. Comput. Chem., 3 (1982) 214-218.
- [56] J.A. Montgomery, M.J. Frisch, J.W. Ochterski, G.A. Petersson, A complete basis set model chemistry. VI. Use of density functional geometries and frequencies, J. Chem. Phys., 110 (1999) 2822-2827.
- [57] P.B. Armentrout, A.L. Heaton, S.J. Ye, Thermodynamics and Mechanisms for Decomposition of Protonated Glycine and Its Protonated Dimer, J. Phys. Chem. A, 115 (2011) 11144-11155.
- [58] A.E. Counterman, D.E. Clemmer, Cis-Trans Signatures of Proline-Containing Tryptic Peptides in the Gas Phase, Anal. Chem., 74 (2002) 1946-1951.
- [59] H.E. Aribi, C.F. Rodriquez, D.R.P. Almeida, Y. Ling, W.W.N. Mak, A.C. Hopkinson, K.W.M. Siu, Elucidation of Fragmentation Mechanisms of Protonated Peptide Ions and Their Products: A Case Study on Glycylglycylglycine Using Density Functional Theory and Threshold Collision-Induced Dissociation, J. Am. Chem. Soc., 125 (2003) 9229-9236. [60] C.F. Rodriquez, A. Cunje, T. Shoeib, I.K. Chu, A.C. Hopkinson, K.W.M. Siu, Proton
- Migration and Tautomerism in Protonated Triglycine, J. Am. Chem. Soc., 123 (2001) 3006-3012.
- [61] J.S. Klassen, P. Kebarle, Collision-Induced Dissociation Threshold Energies of Protonated Glycine, Glycinamide, and Some Related Small Peptides and Peptide Amino Amides, J. Am. Chem. Soc., 119 (1997) 6552-6563.
- [62] E.P.L. Hunter, S.G. Lias, Evaluated Gas Phase Basicities and Proton Affinities of Molecules: An Update, J. Phys. Chem. Ref. Data, 27 (1998) 413-656.
- [63] M.J. Elrod, A comprehensive computational investigation of the enthalpies of formation and proton affinities of C₄H₇N and C₃H₃ON compounds, Int. J. Mass spectrom., 228 (2003) 91-105.

- [64] C.D. Cappa, M.J. Elrod, A computational investigation of the electron affinity of CO₃ and the thermodynamic feasibility of CO₃–(H₂O)_n + ROOH reactions, Phys. Chem. Chem. Phys., 3 (2001) 2986-2994.
- [65] C. Bleiholder, S. Suhai, A.G. Harrison, B. Paizs, Towards Understanding the Tandem Mass Spectra of Protonated Oligopeptides. 2: The Proline Effect in Collision-Induced Dissociation of Protonated Ala-Ala-Xxx-Pro-Ala (Xxx = Ala, Ser, Leu, Val, Phe, and Trp), J. Am. Soc. Mass. Spectrom., 22 (2011) 1032-1039.
- [66] G. Bouchoux, J.Y. Salpin, Gas-Phase Basicity of Glycine, Alanine, Proline, Serine, Lysine, Histidine and Some of Their Peptides by the Thermokinetic Method, Eur. J. Mass Spectrom., 9 (2003) 391-402.
- [67] R.A.J. O'Hair, M.L. Styles, G.E. Reid, Role of the sulfhydryl group on the gas phase fragmentation reactions of protonated cysteine and cysteine containing peptides, J. Am. Soc. Mass. Spectrom., 9 (1998) 1275-1284.
- [68] G.E. Reid, R.J. Simpson, R.A.J. O'Hair, Probing the fragmentation reactions of protonated glycine oligomers via multistage mass spectrometry and gas phase ion molecule hydrogen/deuterium exchange, Int. J. Mass spectrom., 190-191 (1999) 209-230.
- [69] B.J. Bythell, D.F. Barofsky, F. Pingitore, M.J. Polce, P. Wang, C. Wesdemiotis, B. Paizs, Backbone cleavages and sequential loss of carbon monoxide and ammonia from protonated AGG: A combined tandem mass spectrometry, isotope labeling, and theoretical study, J. Am. Soc. Mass. Spectrom., 18 (2007) 1291-1303.
- [70] B. Balta, V. Aviyente, C. Lifshitz, Elimination of water from the carboxyl group of GlyGlyH⁺, J. Am. Soc. Mass. Spectrom., 14 (2003) 1192-1203.
- [71] G.E. Reid, R.J. Simpson, R.A.J. O'Hair, A mass spectrometric and ab initio study of the pathways for dehydration of simple glycine and cysteine-containing peptide [M+H]⁺ ions, J. Am. Soc. Mass. Spectrom., 9 (1998) 945-956.
- [72] A.S. Noguerola, B. Murugaverl, K.J. Voorhees, An investigation of dipeptides containing polar and nonpolar side groups by curie-point pyrolysis tandem mass spectrometry, J. Am. Soc. Mass. Spectrom., 3 (1992) 750-756.
- [73] K.D. Ballard, S.J. Gaskell, Sequential mass spectrometry applied to the study of the formation of "internal" fragment ions of protonated peptides, Int. J. Mass Spectrom. Ion Processes, 111 (1991) 173-189.
- [74] F. Pingitore, M.J. Polce, P. Wang, C. Wesdemiotis, B. Paizs, Intramolecular condensation reactions in protonated dipeptides: carbon monoxide, water, and ammonia losses in competition, J. Am. Soc. Mass. Spectrom., 15 (2004) 1025-1038.
- [75] T. Cooper, E. Talaty, J. Grove, M. Van Stipdonk, S. Suhai, B. Paizs, Isotope labeling and theoretical study of the formation of a₃* ions from protonated tetraglycine, J. Am. Soc. Mass. Spectrom., 17 (2006) 1654-1664.
- [76] J.M. Allen, A.H. Racine, A.M. Berman, J.S. Johnson, B.J. Bythell, B. Paizs, G.L. Glish, Why are a₃ ions rarely observed?, J. Am. Soc. Mass. Spectrom., 19 (2008) 1764-1770.
- [77] G. Fogarasi, P. Pulay, Vibrational Spectra and Structure, Elsevier, New York, 1985.
- [78] A.L. Heaton, P.B. Armentrout, Thermodynamics and Mechanism of Protonated Asparagine Decomposition, J. Am. Soc. Mass Spectrom., 20 (2009) 852-866.
- [79] S.A. Martin, K. Biemann, A comparison of keV atom bombardment mass spectra of peptides obtained with a two-sector mass spectrometer with those from a four-sector tandem mass spectrometer, Int. J. Mass Spectrom. Ion Processes, 78 (1987) 213-228.

Table 1Theoretical energies (kJ mol⁻¹) at 0 K for rate-limiting TSs and products for decomposition of H⁺GPA.^a

Transition state ^b	B3LYP	B3P86		Products	B3LYP	B3P86	MP2
$H^+GPA \rightarrow PSL$				$[b_2]^+ (AMPOx^+) + A$	160	173	209
$TS(H^+GPA[O^1,N^1-N^3])$	263	249	258	$[b_2]^+ (H^+DKP) + A$	111	119	156
$TS(H^+GPA[N^1-O^4]) \to [b_3]^+$	148	147	144	$[b_3]^+ \left(H^+GPMOx\right) + H_2O$	112	117	130
$TS(H^+GPA[N^2]) \rightarrow [y_2+2H]^+$	164	194	197	$[y_2+2H]^+(H^+PA) + CO + CH_2NH$	139	190	185
$H^+GPA \to PSL$				$[a_1]^+ (CH_2NH_2^+) + CO + PA$	265	315	308
$[b_3]^+ \rightarrow TS(H^+GPMOx)$	228	256	245	$[a_3]^+ (C_9H_{16}N_3O_2^+) + H_2O + CO$	148	195	180
$[b_2]^+ \rightarrow TS(AMPOx^+\{C \sim CO^2 \sim O^1\})$	268	302	312	$[a_2]^+ (C_6H_{11}N_2O^+) + CO + A$	196	251	254
$[a_3]^+ \rightarrow PSL$				$AMPOx^{+} + C_2H_4NH + H_2O + CO$	256	313	316
$[a_2]^+ \to TS([a_2]^+ \{N^2 \sim CO^1 \sim C\})$	306	391	381	$C_4H_7NH^+ + CH_2NH + 2CO + A$	277	378	361
$[a_2]^+ \rightarrow PSL$				$[a_1]^+(CH_2NH_2^+)+C_4H_7N+2CO+A$	349	449	424
$[y_2+2H]^+ \to TS([y_2+2H]^+\{C\sim CO^2\sim N^3\})$	301	374	361	$C_4H_7NH^+ + CH_2NH + 2CO + A$	277	378	361
$[y_2+2H]^+ \to PSL$				$H^{+}A + C_{4}H_{7}N + CH_{2}NH + 2CO$	313	411	389
$TS(H^+GPA\text{-}CO[N^2\text{-}N^1]) \to CH_2PA^+$	174	197	181	$CH_2PA^+ + CO + NH_3$	129	181	156

 $[\]begin{array}{l} {}^{a} \ Rate\text{-limiting TS in bold.} \ {}^{b} \ PSL = phase \ space \ limit.} \ TS(H^{+}GPA[O^{1},N^{1}\text{-}N^{3}]) = TS(H^{+}GPA[O^{1},N^{1}\text{-}N^{3}]\text{-}(gc)c(gc)tgttt\{CO^{2}\sim N^{3}\}). \\ TS[N^{1}\text{-}O^{4}] = TS(H^{+}GPA[N^{1}\text{-}O^{4}]\text{-}(gt)cgttcgt\{C\sim O^{4}H\}). \ TS(H^{+}GPA[N^{2}]) = TS(H^{+}GPA[N^{2}]\text{-}gtgttgtt\{N^{1}C\sim CO^{1}\sim N^{2}C\}). \ TS(H^{+}GPMOx) \\ = TS(H^{+}GPMOx[N^{3}]\text{-}gtggtt)\{C\sim CO^{3}\}). \ TS([y_{2}\text{+}2H]^{+}\{C\sim CO^{2}\sim N^{3}\}) = TS([y_{2}\text{+}2H]^{+}[N^{2}]\text{-}cggtt\{C\sim CO^{2}\sim N^{3}\}). \end{array}$

Table 2 Theoretical energies (kJ mol⁻¹) at 0 K for the TSs, intermediates, and products for decomposition of AMPOx⁺ and H⁺DKP.^a

Species ^b	$AMPOx^+$		$H^+DKP (N^2CO^1)^c$			$H^+DKP (N^1CO^2)^d$			
	B3LYP	B3P86	MP2	B3LYP	B3P86	MP2	B3LYP	B3P86	MP2
$[b_2]^+ \to TS(H^+DKP[O^1-N^{1,2}])$	N/A	N/A	N/A	(339)	342	<u>377</u>	(353)	<u>352</u>	380
$[b_2]^+$ (+ charge on $N^{1,2}$)	160	173	209	171	183	204	186	198	220
$[b_2]^+ \to TS\{X \sim CO^{2,1} \sim C\}$	<u>268</u>	<u>302</u>	<u>312</u>	307	<u>346</u>	353	258	293	305
$[a_2]^+$ •CO	182	238	236	271	326	317	188	243	239
$[a_2]^+ + CO$	196	251	254	246	300	298	e	e	e
$[a_2]^+ \to TS\{N^{2,1} \sim CO^{1,2} \sim C\}$	(306)	(391)	(381)	317	(394)	(388)	e	e	e
$(C_4H_7N)H^+(CH_2NH)$ •CO	188	285	256	189	286	257	192	289	261
$(C_4H_7N)H^+(CH_2NH)+CO$	196	292	268	e	e	e	e	e	e
$C_4H_7NH^+ + CH_2NH + CO$	277	378	361	e	e	e	e	e	e
$CH_2NH_2^+([a_1]^+) + pyr + CO$	349	449	424	e	e	e	e	e	e

^a All energies are relative to H⁺GPA GS. Rate-limiting TS for [a₂]⁺ formation underlined. Rate-limiting TS for H⁺(pyr) formation in parentheses. Rate-limiting TS for [a₁]⁺ formation in bold.

Superscripts separated by a comma refer to the H⁺DKP (N¹CO²) and H⁺DKP (N²CO¹) pathways. TS{X~CO^{2,1}~C} = TS(AMPOx⁺{C~CO²~O¹) for the Oxa pathway and TS(H⁺DKP{N^{1,2}~CO^{2,1}~C}) for the H⁺DKP pathways.

^c Pathway where N² is protonated and CO¹ is lost first.

^d Pathway where N¹ is protonated and CO² is lost first.

^e Energies are equivalent to those of AMPOx⁺.

Table 3 Fitting Parameters for Eqs. (S1), (S3a), and (S3b) with Threshold Energies at 0 K and Entropies of Activation at 1000 K for the Decomposition of H⁺GPA and [b₂]⁺.

Ionic	Products	Transition State ^a	σ_0	n	E_0	$\Delta\mathcal{S}_{1000}{}^{\dagger}$
Reactant					(eV)	$(J K^{-1} mol^{-1})$
H ⁺ GPA	$[b_2]^+ (AMPOx^+) + A$	PSL	22.0 ± 3.1	1.2 ± 0.2	2.16 ± 0.05	114 ± 5
	$[b_3]^+ (H^+GPMOx) + H_2O$	$TS[N^1-O^4]^b$	22.0 ± 3.1	1.2 ± 0.2	1.62 ± 0.04	44 ± 4
	$[y_2 + 2H]^+ (H^+PA) + CO + CH_2NH$	$TS[N^2]^c$	22.0 ± 3.1	1.2 ± 0.2	2.11 ± 0.06	146 ± 5
	$[a_1]^+ (CH_2NH_2^+) + CO + PA$	PSL	22.0 ± 3.1	1.2 ± 0.2	3.06 ± 0.07	204 ± 5
	$[a_2]^+ + A + CO$	$TS(AMPOx^{+}\{C\sim CO^{2}\sim O^{1}\})$	22.0 ± 3.1	1.2 ± 0.2	3.25 ± 0.10	22 ± 18
	$[a_3]^+ + H_2O + CO^d$	$TS(H^+GPMOx)$	10.9 ± 1.3	2.1 ± 0.1	2.54 ± 0.13	30 ± 61
$[b_2]^+$	$[a_2]^+ + CO$	$TS(AMPOx^{+}\{C\sim CO^{2}\sim O^{1}\})$	21.2 ± 18.6	1.4 ± 0.6	1.24 ± 0.14	22 ± 1
	$C_4H_7NH^+ + CH_2NH + 2CO$	$TS([a_2]^+{N^2\sim CO^1\sim C})$	21.2 ± 18.6	1.4 ± 0.6	2.58 ± 0.16	57 ± 16
	$[a_1]^+ (CH_2NH_2^+) + C_4H_7N + 2CO$	PSL	21.2 ± 18.6	1.4 ± 0.6	2.90 ± 0.16	72 ± 14

 $^{^{}a}PSL = phase \ space \ limit. \ TS[N^{1}-O^{4}] = TS(H^{+}GPA[N^{1}-O^{4}] - (gt)cgttcgt\{C \sim O^{4}H\}). \ TS[N^{2}] = TS(H^{+}GPA[N^{2}] - gtgttgtt\{N^{1}C \sim CO^{1} \sim N^{2}C\}).$ TS(H⁺GPMOx) = TS(H⁺GPMOx[N³]-gtggtt{ $C\sim CO^3$ }). ^b Frequencies below 900 cm⁻¹ scaled by 0.825.

^c Frequencies below 900 cm⁻¹ scaled by 0.75.

^d Fit of high-pressure data leading to different N value. $E_0 = 2.05 \pm 0.02$ eV before adjusting for pressure dependence.

Table 4Comparison of experimental and theoretical reaction energies (kJ mol⁻¹) at 0 K for decomposition of H⁺GPA.

Reactant	Products	Transition state ^a	Exp ^b this work	Theory ^c		
				B3LYP	B3P86	MP2
H ⁺ GPA	$[b_2]^+ (AMPOx^+) + A$	PSL	206 ± 5	160	173	209
	$[b_3]^+ (H^+GPMOx) + H_2O$	$TS[N^1-O^4]$	156 ± 4	148	147	144
	$[y_2 + 2H]^+ (H^+PA) + CO + CH_2NH$	$TS[N^2]$	203 ± 6	164	194	197
	$[a_1]^+$ (CH ₂ NH ₂ ⁺) + CO + PA	PSL	$>295\pm7$	265	315	308
	$[a_2]^+ (C_6H_{11}N_2O^+) + A + CO$	$TS(AMPOx^{+}\{C{\sim}CO^{2}{\sim}O^{1}\}$	310 ± 10	268	302	312
	$[a_3]^+ (C_9H_{16}N_3O_2^+) + H_2O + CO^d$	$TS(H^+GPMOx)$	245 ± 13	228	256	245
AMPOx ⁺	$[a_2]^+ (C_6H_{11}N_2O^+) + CO$	$TS(AMPOx^{+}\{C\sim CO^{2}\sim O^{1}\})$	119 ± 14	109	130	103
	$H^{+}(pyr)(C_4H_7NH^{+}) + CH_2NH + 2CO$	$TS([a_2]^+\{N^2\sim CO^1\sim C\})$	<249 ± 16	146	219	172
	$[a_1]^+$ (CH ₂ NH ₂ ⁺) + C ₄ H ₇ N + 2CO	PSL	<280 ± 16	189	276	216
	MAD ^e			28 ± 16	14 ± 9	8 ± 6

^a PSL = phase space limit. TS[N¹-O⁴] = TS(H⁺GPA[N¹-O⁴]-(gt)cgttcgt{ $C\sim O^4H$ }). TS[N²] = TS(H⁺GPA[N²]-gtgttgtt{ $N^1C\sim CO^1\sim N^2C$ }). TS(H⁺GPMOx) = TS(H⁺GPMOx[N³]-gtggtt{ $C\sim CO^3$ }).

^b Experimental E_0 values are taken from Table 3.

^c Computational results using a 6-311+G(2d,2p) basis set and corrected for ZPE.

^d Threshold information collected at high pressure and extrapolated to zero-pressure conditions based on average threshold different between high and zero-pressure conditions for other channels.

^e Mean absolute deviation (MAD) from experimental threshold energies for $[b_2]^+$, $[b_3]^+$, $[y_2 + 2H]^+$, $[a_1]^+$, $[a_2]^+$, and $[a_3]^+$ from H⁺GPA and $[a_2]^+$ from AMPOx⁺.

Figure Captions

Fig. 1. Cross sections for the decomposition of H⁺GPA by collision with Xe at 0.12 mTorr as a function of kinetic energy in the center-of-mass (CM) frame (lower x-axis) and the laboratory frame (lab) (upper x-axis). Mass-to-charge ratios and explicit nomenclature are given to identify all products present. Closed symbols represent fragments that are predominantly primary products and open symbols represent fragments formed by sequential dissociation from the precursor having the same color and symbol. The solid black line represents the total cross section, and the green dashed line shows the sum of the $[b_2]^+$, $[a_2]^+$, and H^+ (pyr) cross sections.

Fig. 2. Cross sections for the decomposition of the H⁺GPA [b₂]⁺ fragment by collision with Xe extrapolated to zero pressure as a function of kinetic energy in the center-of-mass (CM) frame (lower x-axis) and the laboratory frame (lab) (upper x-axis). Mass-to-charge ratios and explicit nomenclature are given to identify all products present. Small dots represent the total cross section. Full lines show the models of Supplementary Eqs. (S1), (S3a), and (S3b) for the [a₂]⁺ primary channel and two secondary fragments resulting from further decomposition including convolution over the kinetic and internal energy distributions of the reactants. Dashed lines represent the models in the absence of such broadening with internal energies at 0 K.

Fig. 3. Low-lying H⁺GPA conformers and the *cis/trans* isomerization TS with relative energies in kJ mol⁻¹ calculated at the B3LYP, B3P86, and MP2 levels of theory, respectively.

Fig. 4. Key transition states and products for H⁺GPA decomposition. Dashed lines denote making and breaking of bonds. TS(H⁺GPA[N²]-gtgttgtt{N¹C~CO¹~N²C}) is the rate-limiting decarbonylation TS for $[y_2 + 2H]^+$ formation. TS(H⁺GPA[N¹-O⁴]-(gt)cgttcgt{C~O⁴H}) is the rate-limiting dehydration step for $[b_3]^+$ formation. TS(H⁺GPMOx[N³]-gtggtt{C~CO³}) is the rate-limiting decarbonylation TS for $[a_3]^+$ formation from $[b_3]^+$. TS(AMPOx⁺{C~CO²~O¹}) is the rate-

limiting decarbonylation TS for $[a_2]^+$ formation from $[b_2]^+$. TS($[a_2]^+$ {N²~CO¹~C}) is the rate-limiting decarbonylation TS for C₄H₇NH⁺ formation from $[a_2]^+$.

Fig. 5. Key transition states and products for H⁺DKP formation and decomposition. Dashed lines denote making and breaking of bonds. TS(H⁺GPA[O¹,N¹N³]-(gc)c(gc)tgttt N¹~CO²~N³}) is the rate-limiting TS for H⁺DKP formation.

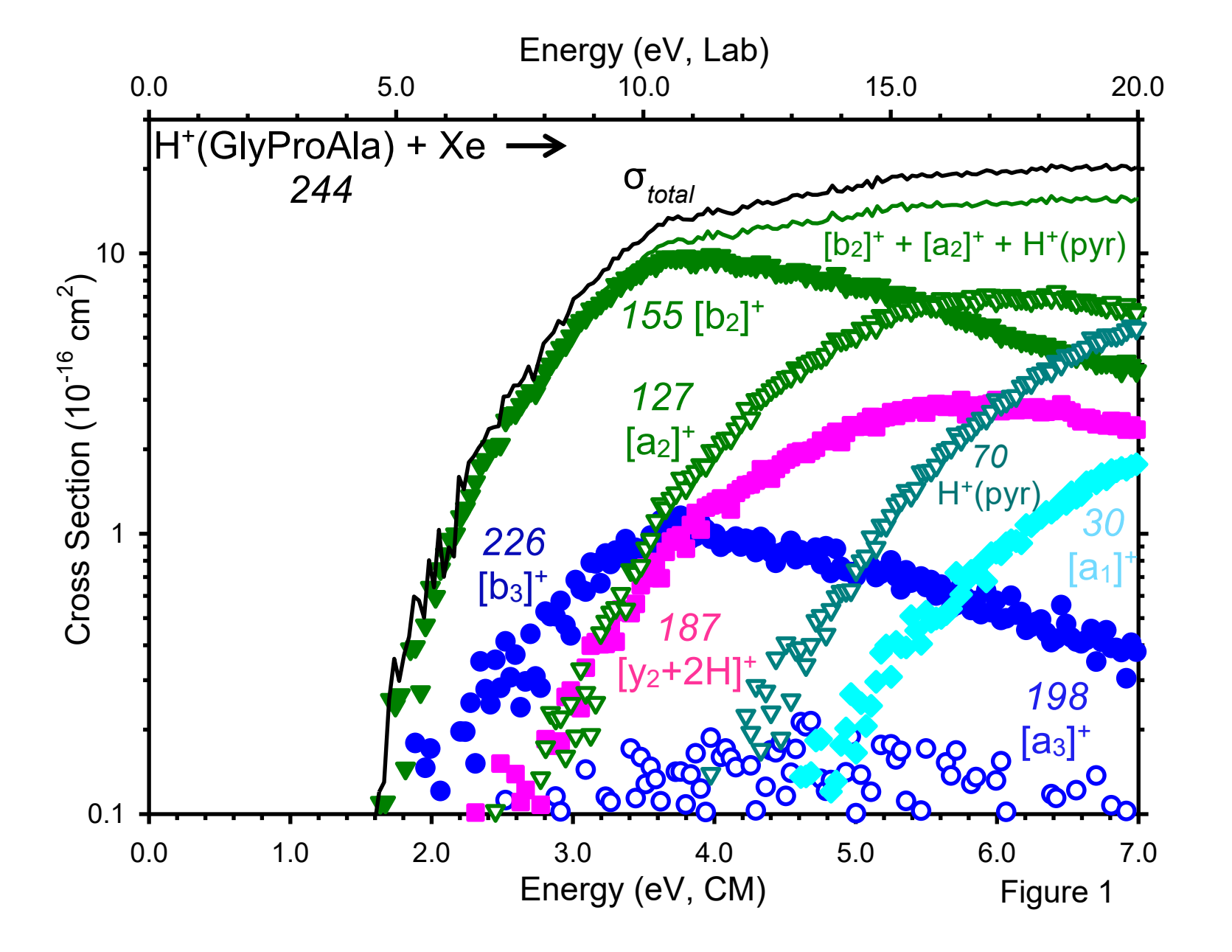
Fig. 6. Cross sections for the decomposition of H⁺GPA by collision with Xe extrapolated to zero pressure as a function of kinetic energy in the center-of-mass (CM) frame (lower x-axis) and the laboratory frame (lab) (upper x-axis). Mass-to-charge ratios and explicit nomenclature are given to identify all products present. Closed symbols represent fragments that are predominantly primary products and open symbols represent fragments formed by sequential dissociation from the precursor having the same color and symbol. Full lines show the models of Supplementary Eqs. (S1), (S3a), and (S3b) for four primary channels and the secondary [a₂]⁺ fragment resulting from decarbonylation of the [b₂]⁺ fragment including convolution over the kinetic and internal energy distributions of the reactants. Dashed lines represent the models in the absence of such broadening with internal energies at 0 K.

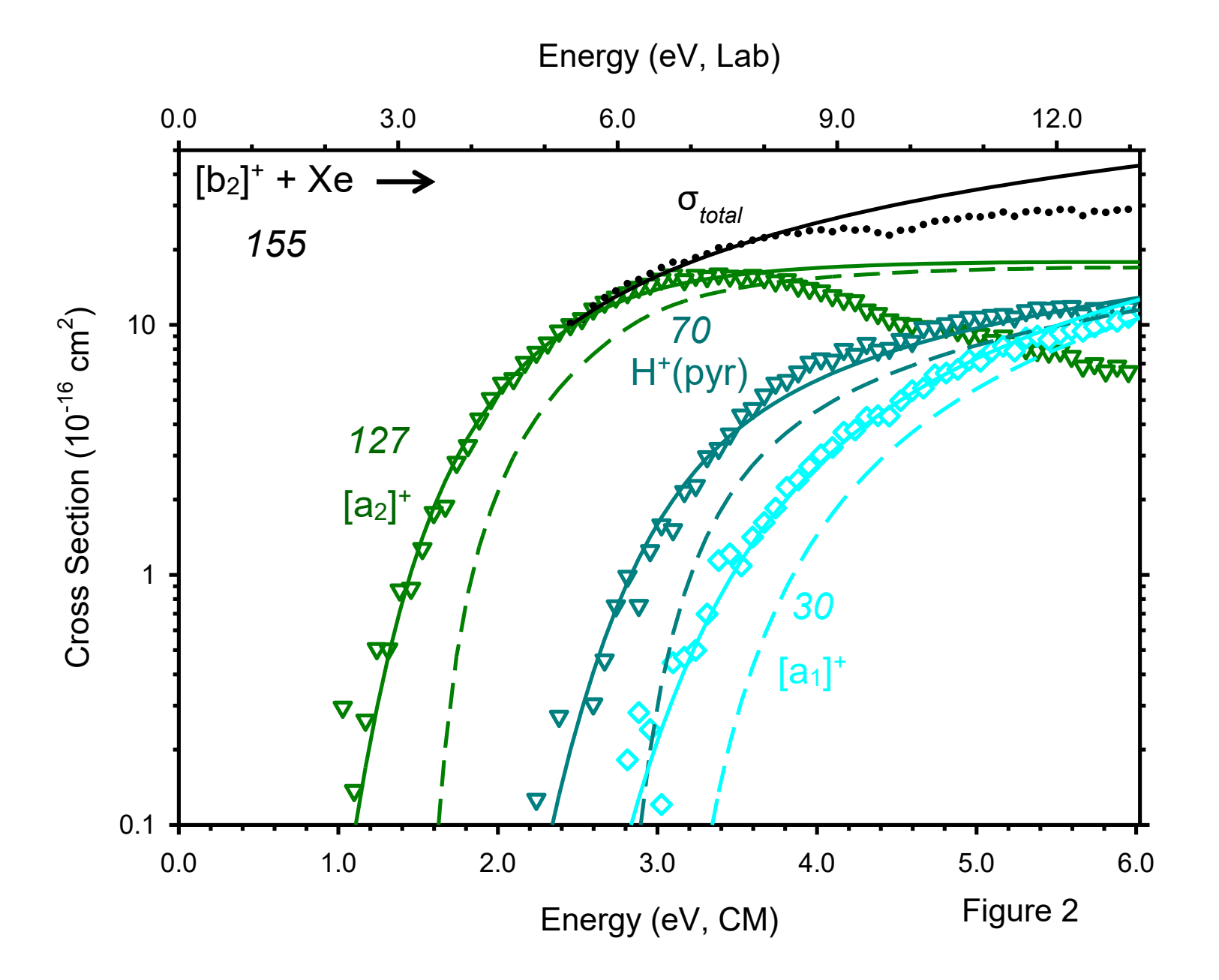
Fig. 7. Comparison of experimentally determined energy thresholds for decomposition of H⁺GPA (open symbols) and AMPOx⁺ (closed symbols) with B3P86 (blue squares), B3LYP (green triangles), MP2 (red circles) levels of theory. The black diagonal line indicates complete agreement between experimental and theoretical values.

Scheme 1. Schematic reaction mechanism for the decomposition of H⁺GPA. Observed products are in bold.

Scheme 2. Schematic reaction mechanism for the decomposition of H⁺DKP and AMPOx⁺.

Scheme 1





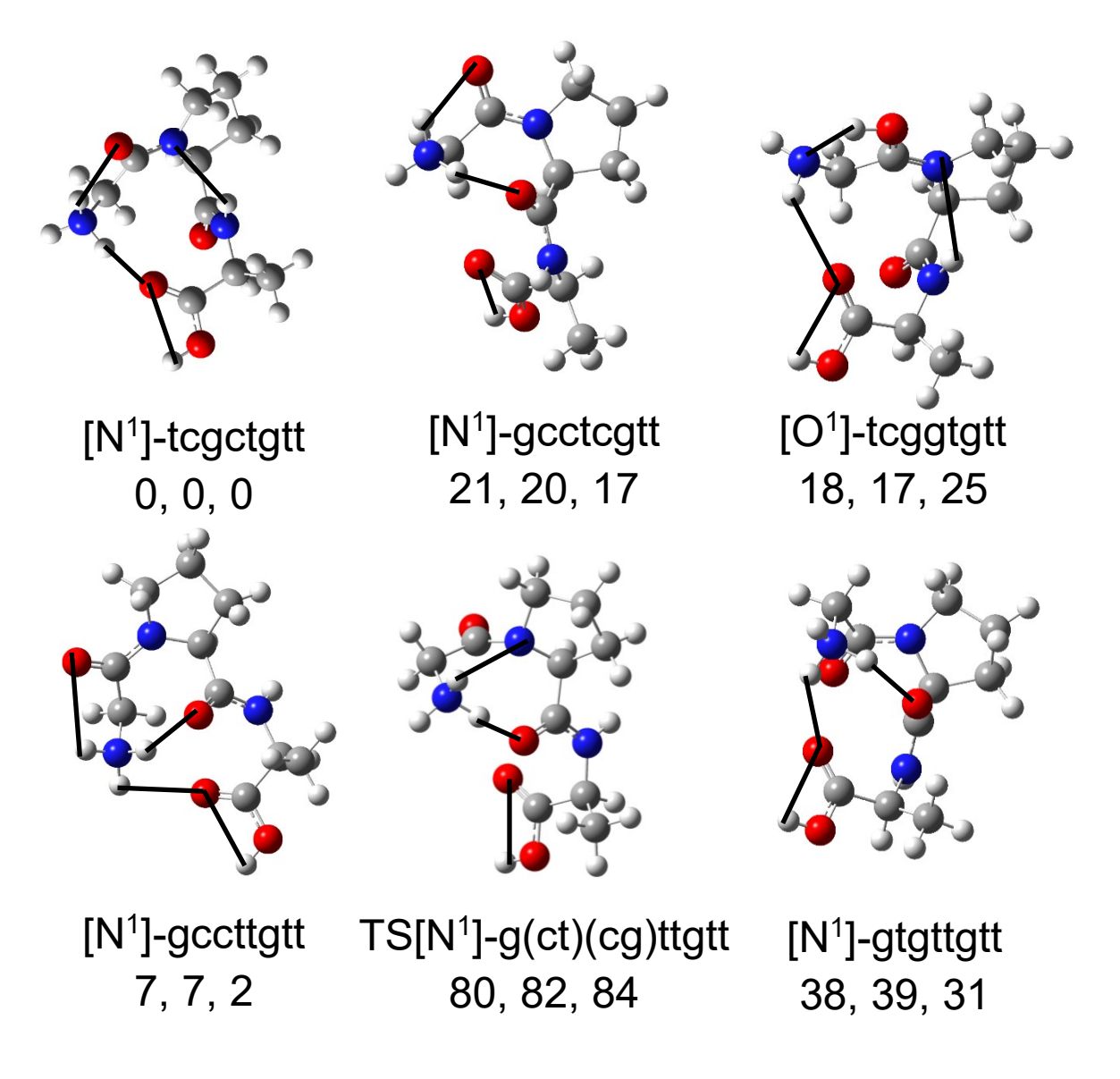


Figure 3

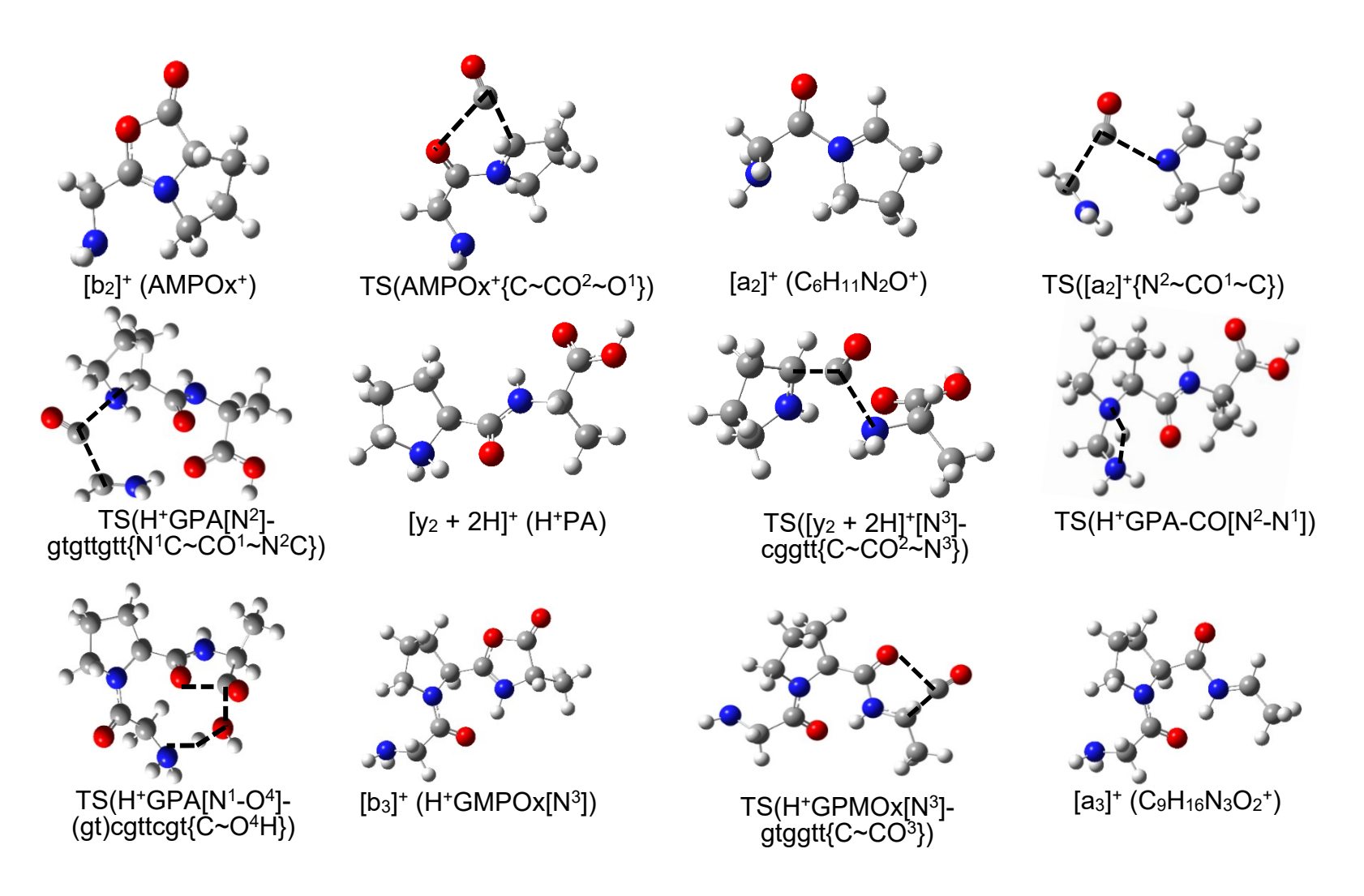


Figure 4

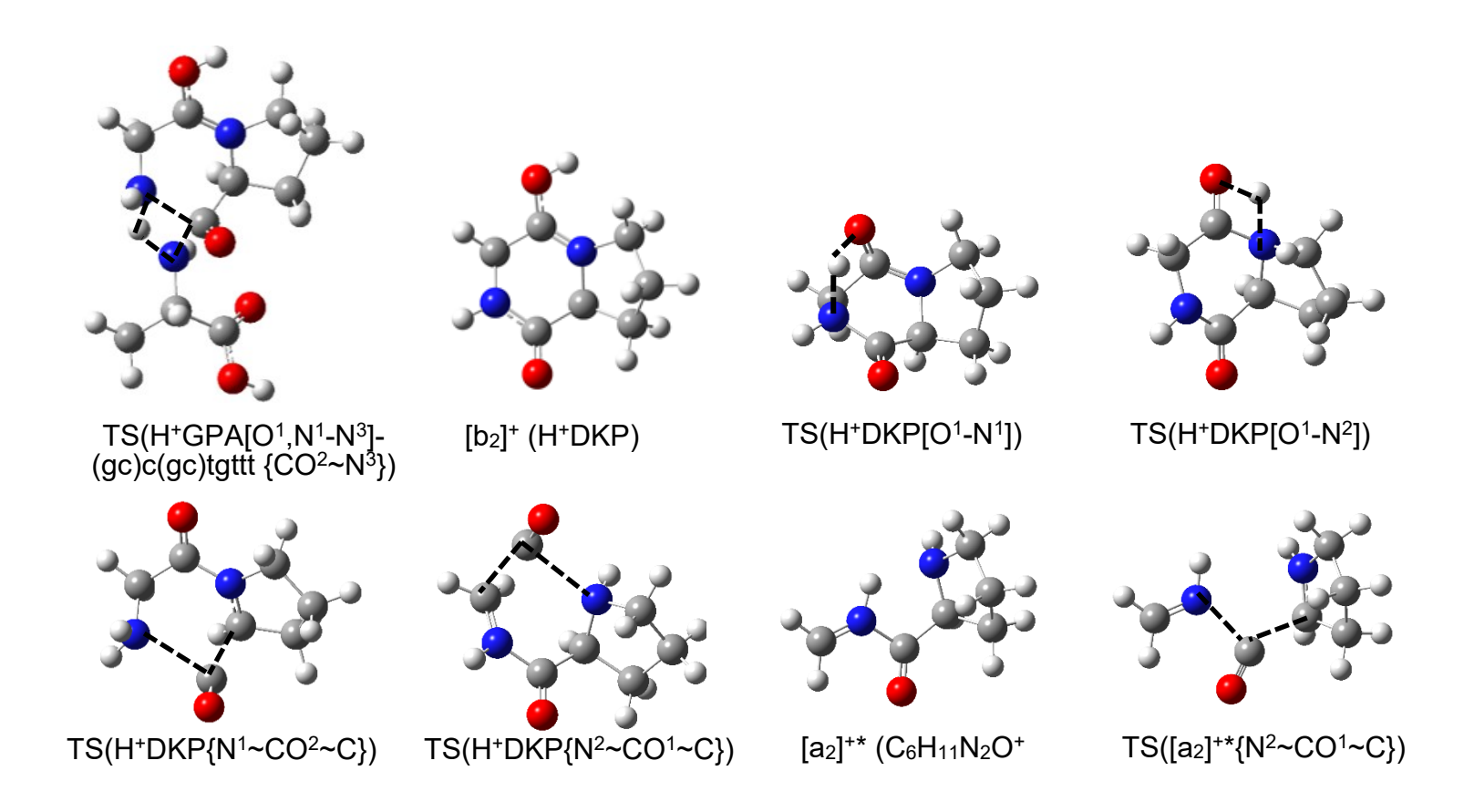
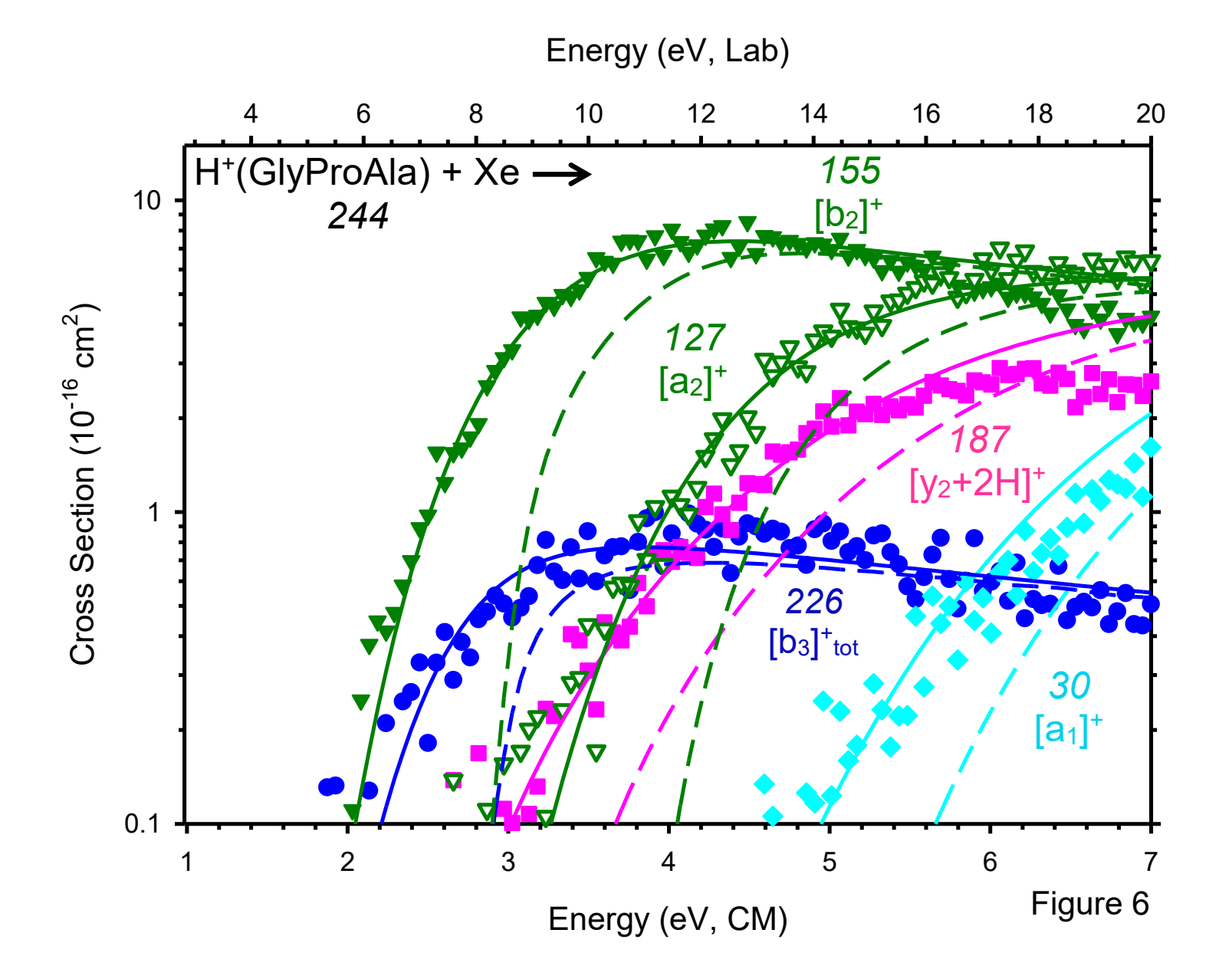


Figure 5



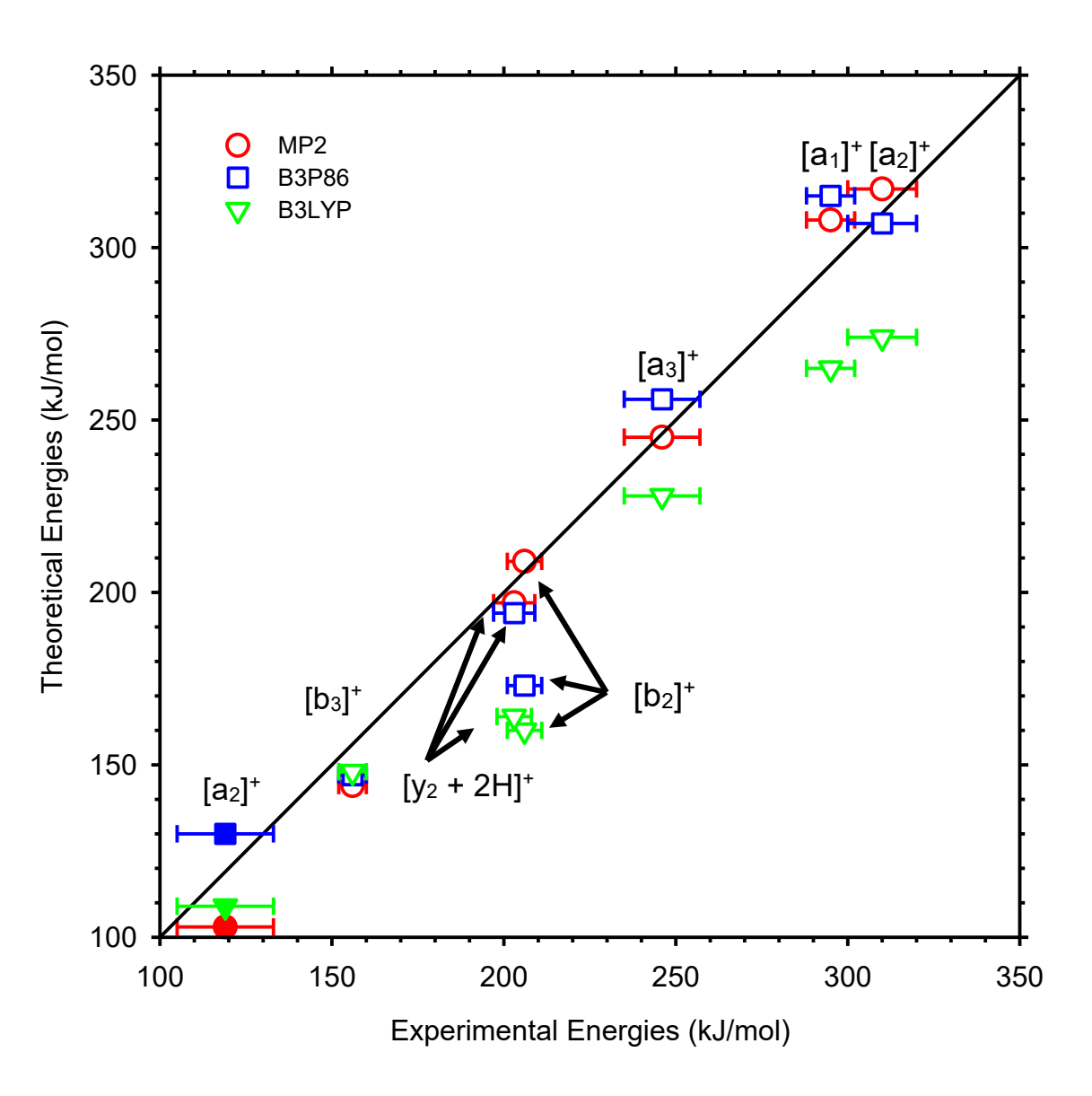


Figure 7